Internal Pressure Gradient Errors in σ-coordinate Ocean Models:

The Finite Volume and Weighted Approaches

Master thesis in Applied and Computational Mathematics

Helene Hisken Pedersen

Department of Mathematics

University of Bergen

April 27, 2010

Acknowledgements

First of all, I wish to thank my supervisor Jarle Berntsen for all enthusiasm, help and support, and for making me feel that my work is important.

Secondly, I would like to thank all my excellent friends and fellow students (and fellow adventurers!), who have made my years at the university absolutely fantastic.

Thank you, Gunn Inger, for all the late night talks, Torbjørg for our amazingly lazy ski-trips, Christin, for proving that everything is possible, and Elise, for being the other half of our dynamic duo for all these years.

Gunnhild, thank you for caring so much. Borghild – think of all the brown cheese sandwiches and giggling we have shared! Being a student would have been so much duller without you.

Thank you for being the funniest person alive, Marianne. And thanks to my parents, for giving me the best childhood I could have had.

Last, but not least, I would like to thank my wonderful boyfriend Anders for still liking me.

<div align="right">

Helene Hisken Pedersen
Bergen, April 27 2010

</div>

Contents

Introduction

The vast water masses that cover about 71 percent of the world, represent an enormous and complex ecosystem. Apart from being an important food resource, the ocean has made much of the modern world's transport and trade possible. The climate changes that are currently faced are closely connected with the rise of the sea level. The consequences will probably affect millions ['ocean', 2010].

A numerical model that successfully reproduces the processes of the ocean is therefore an invaluable tool in climate and environmental studies, ocean forecasting, and for all of the industries that are in any way dependent on the existence of the sea. The improvements in computer science make it possible to continuously do more complex studies.

A classification of ocean models

Most of the 3-D ocean general circulation models of today can be divided into three different classes, characterised by their respective treatment of the vertical coordinates [Haidvogel and Beckmann, 1999].

The earlier ocean models utilised geopotential *z-coordinates* in the vertical, for instance the Geophysical Fluid Dynamics Laboratory (GFDL) model from the late 1960's [Bryan and Cox, 1968]. A more recent example is the Hamburg Shelf Ocean Model (HAMSOM) [Backhaus and Hainbucker, 1987].

In z-coordinates, the equations appear on their standard form, so that no transformations are required, see Figure 1. This leads to a simple computation of the pressure terms, which clearly is a favourable aspect. However, the geopotential coordinates lead to problems with the resolution of the surface and bottom boundary layers. At the bottom, a varying topography will result in a staircase-shaped boundary, which can cause $2\Delta x$ noise and artificial divergence/convergence. In addition, the diapycnal diffusion is difficult to resolve, since the vertical coordinates of the model are along iso-surfaces of constant depth [Haidvogel and Beckmann, 1999].
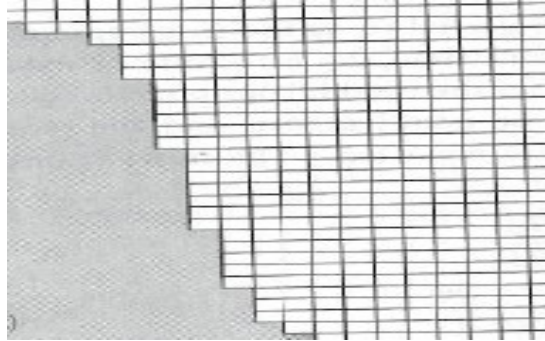
Figure 1: The z-coordinates, picture taken from [Haidvogel and Beckmann, 1999].
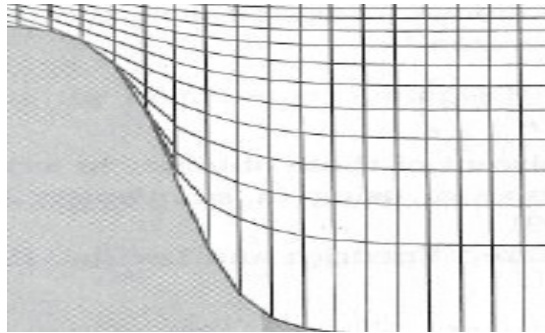
Figure 2: Example of isopycnal coordinates, picture taken from [Haidvogel and Beckmann, 1999].

During the 1970's, the concept of *density layer models* with *isopycnal coordinates* was introduced. The models of this class consist of a number of immiscible layers that are free to adjust, i.e. the vertical grid is time-dependent, see Figure 2. An example is the Miami Isopycnic Model (MICOM) [Bleck and Smith, 1990].

The use of isopycnal coordinates leads to high resolution in the vertical density gradients, and does not cause false diapycnal mixing. Transport in the ocean appear mainly along the isopycnal surfaces. Meanwhile, the resolution of the surface layer can be poor, since the layer has a tendency to become very thick. The bottom boundary layer is also difficult to resolve with

these coordinates. In addition, the isopycnal coordinate transformation leads to an error in the internal pressure gradient. This error will be thoroughly addressed below.

Models using *terrain-following coordinates* in the vertical entered the scene at the same time as the diapycnal approach. These vertical coordinates are fixed in time, but follow the underlying topography, see Figure 3. Terrain-following models are widely used today, e.g. the σ-coordinate Princeton Ocean Model (POM) [Blumberg and Mellor, 1987] and the s-coordinate Rutgers University Model (SCRUM) [Song and Haidvogel, 1994]. In this study, focus will be on the σ-coordinate system.
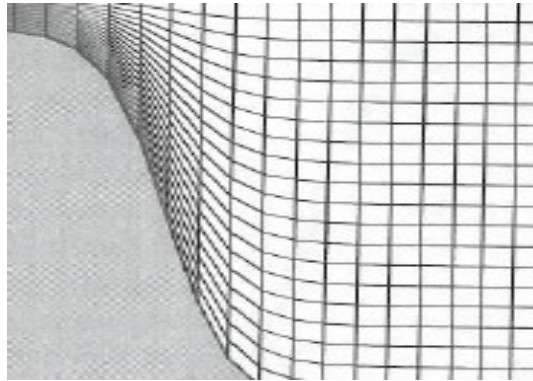
Figure 3: An example of the terrain-following approach: σ-coordinates with equidistant layers, taken from [Haidvogel and Beckmann, 1999]. Note how fine the resolution in the shallow is.

The σ-coordinates are advantageous when dealing with large variations in topography. The bottom and top boundary layers are represented accurately. However, in areas of steep topography, the use of these coordinates can lead to a large error in the pressure gradient force.

The internal pressure gradient problem

After the transformation, the horizontal pressure gradient in the σ-coordinate system consists of two terms which often are large, comparable in magnitude, and opposite in sign. The numerical error resulting from the discretisation of these terms can ultimately lead to an unacceptable result. The analytical form of the equation, and the choice of numerical scheme, will naturally affect the error. A solution to this problem would undoubtedly strengthen

the position of the σ-coordinate models, and be a significant contribution to the many advantages of the terrain-following approach.

The severity of the pressure gradient error is currently a topic of discussion. Haney [1991] introduced the concept of *hydrostatic consistency*. A scheme is said to be hydrostatically consistent if

$$\left| \frac{\sigma}{\delta\sigma} \frac{\delta D}{D} \right| < 1 \,. \tag{1}$$

Here, σ is the vertical sigma coordinate, $\delta\sigma$ is the vertical grid size, δD is the horizontal change of depth between two neighbouring cells and $D = H + \eta$ where H is the static depth and η is the free surface elevation. Note that the condition (1) will not be satisfied closer to the bottom boundary if $\delta\sigma$ is small.

For this reason, Mellor et al. [1994] argued that criterion (1) is quite restrictive. Furthermore, they derived the discretisation error for the second-order internal pressure method used in the POM. To leading order, the error is given by

$$E\left(\frac{\delta_x b}{\delta x} \right) = \frac{D}{4} \frac{\delta_x D}{\delta x} \left(\frac{\partial^2 b}{\partial z^2} \right) \left[(\delta\sigma)^2 - \sigma^2 \left(\frac{\delta_x D}{D} \right)^2 \right] \,, \tag{2}$$

where x is the horizontal coordinate, z is the vertical coordinate, $b = \frac{\rho g}{\rho_0}$ is the buoyancy, g is the gravity constant, ρ is the density, and ρ_0 is a constant reference density. In contrast to (1), equation (2) shows that the error decreases if $\delta\sigma$ and $\frac{\delta_x D}{D}$ goes to zero, see [Berntsen and Oey, 2010]. In other words, hydrostatic consistency is not a particularly meaningful concept – increasing the vertical resolution will not reduce the error if the term involving $\frac{\delta_x D}{D}$ is the limiting factor. After observing that the error was not numerically divergent, Mellor et al. [1994] concluded that the internal pressure gradient problem was not of great concern.

Simple test cases can enable the investigator to measure the internal pressure error. By choosing an appropriate function for the density ρ, it is possible to find an analytical solution to the problem. For example, Haney [1991] studied geostrophic flow.

Beckmann and Haidvogel [1993] introduced the seamount case; a rectangular test basin featuring a tall, narrow peak. For horizontal isopycnals, the horizontal pressure gradient force should always equal zero. In such cases, possible errors can easily be identified as artificial velocities. Beckmann and Haidvogel experienced growing errors for some of their seamount experiments.

In 1998, Mellor et al. used the POM to study the seamount case. They classified the errors from the 1994 paper as Sigma Errors of the First Kind (SEFK), and related them to 2D problems. According to Mellor et al. [1998], the SEFK will eventually die out. The growing errors in [Beckmann and Haidvogel, 1993] were classified as Sigma Errors of the Second Kind (SESK). Mellor et al. related these to the vorticity – relevant to 3D cases. The SESK they observed decayed to a nonzero value.

Possible remedies

A significant amount of approaches have been developed for the purpose of reducing the internal pressure gradient error. For instance, it is common to subtract the background stratification that depends only on z from the density field [Gary, 1973]. One can argue that this will make the remaining terms in the equation smaller, and therefore lead to a reduced truncation error [Gary, 1973], [Haney, 1991]. However, since the "correct" way of splitting the density field is unknown, the validity of these manipulations can be questioned [Shchepetkin and McWilliams, 2003].

Even though the SESK are limited in the case treated by Mellor et al. [1998], several later studies have suggested that the error term may grow strongly in cases where more realistic viscosities are applied [Berntsen, 2002]. Adding viscosity will certainly dampen the artificial flow, yet it is desirable to have ocean models that are able to represent situations as realistically as possible.

Stelling and Van Kester [1994] proposed computing the internal pressure in z-coordinates. By interpolation, they made two estimates of the horizontal pressure gradient, and set it to zero when the results were of opposite signs. If the estimates were of the same sign, the smaller term was used. While this approach guarantees accurate results for the horizontal pycnoline seamount case, Slørdal [1997] found that it will generally underestimate the true geostrophic flow .

Song [1998] advocated the use of a Jacobian representation of the pressure gradient term. He pointed out that applying the gradient before the integration may reduce the truncation error of the scheme.

It is also possible to smooth the topography of the area of study [Barnier et al., 1998], and by this directly removing the cause of the error. However, altering the topography too much would mean solving the equations for a different case than the one in question.

Numerical methods

Much effort has been put into improving the numerical method used to compute the internal pressure. In 1994, McCalpin addressed the seamount case using a fourth order method. Chu and Fan [1997] showed that the error can be further reduced by applying a sixth order method. However, they concluded that there will be little advantage to using the sixth order scheme if the bathymetry is not complex.

In [Shchepetkin and McWilliams, 2003], the area integrals of the pressure are transformed to line integrals using Green's theorem. The line integrals are evaluated using integrations of polynomial fits of the integrands. Shchepetkin and McWilliams reported results that were superior to the second order POM method. Meanwhile, Berntsen and Oey [2010] questioned if this improvement was indeed due to the new approach, or if the increased order was the most important factor. They found that the POM approach generally gave better results when methods of corresponding order were compared.

In 2006, Thiem and Berntsen calculated the internal pressure gradient in a grid that was rotated 45 degrees [Thiem and Berntsen, 2006]. The new pressure gradient was then weighted with the standard second order POM method, using a fixed constant. For some weights this gave a reduced error, implying that there could be some error term cancellation at work.

The focus of this study

Finite volume methods

Using finite differences is the traditional way of discretising the equations. It is simple and efficient. However, it is possible to integrate over finite volumes instead. The finite volume approach discretises the integral form of the equation. For conservation laws, it is advantageous to find numerical methods based on their integral form [LeVeque, 2002], and the laws of ocean dynamics are expressed as conservation of quantities in a unit volume. In the model FVCOM, the finite volume approach is combined with an unstructured grid [Chen et al., 2003].

In this study, the traditional computation of the internal pressure in the Princeton Ocean Model [Blumberg and Mellor, 1987] will be interpreted as a finite volume method. New points will be included, so as to take it to higher order. Some of the methods will also be combined with the weighted rotated grid approach from [Thiem and Berntsen, 2006].

The optimal weighting

Weighting of different approaches is an idea often used in advanced shock-capturing schemes. So-called flux-limited schemes are constructed as a combination of a low order and a high order approximation [Yang and Przekwas, 1992]. The weighting can be constructed in such a way that the TVD (total variation diminishing) property is satisfied, e.g. the Superbee limiter technique [Roe, 1986]. For example, a TVD-scheme with a Superbee limiter is an option for advection in the Bergen Ocean Model (BOM) [Berntsen, 2000].

The finite volume methods developed here will all have fixed weights. Inspired by the varying weights in the TVD-scheme, an optimal weighting for the internal pressure gradient computation will be introduced. The weights will be computed such that the internal pressure errors are minimised, and will depend on the topography, the stratification, and the grid size.

All methods will be applied to an idealised test case - the seamount problem.

Chapter 1

Underlying equations and approximations

The before mentioned numerical models are all built on the laws of fluid flow. However, ocean models in general represent a wide array of applied approximations, parametrisations and discretisations.

In the following, the well-merited σ-coordinate Princeton Ocean Model (POM) [Blumberg and Mellor, 1987] will be used for all experiments. Some of the basic principles that the POM is based on will be established, especially focusing on the pressure term.

This chapter has been worked out in collaboration with Borghild Ness [Ness, 2010].

1.1 The basic laws of fluid flow

Mass and momentum should always be conserved. Conservation of mass can be expressed as

$$\frac{\partial \rho}{\partial t} + \nabla \cdot (\rho \mathbf{V}) = 0 \ . \tag{1.1}$$

This is called *the equation of continuity*. As for momentum, Newton's second law for fluids can be stated as

$$\frac{D\mathbf{V}}{Dt} = -\frac{1}{\rho} \nabla p - 2\mathbf{\Omega} \times \mathbf{V} + \mathbf{g} + \mathbf{F} \ , \tag{1.2}$$

where $\mathbf{V}$ is the velocity field $[u, v, w]$, ρ is the density, p is the pressure, $\mathbf{\Omega}$ is the earth rotation vector, $\mathbf{g}$ is the gravity, $\mathbf{F}$ represents other forces, and $\frac{D}{Dt}$

is the total derivative operator. The earth rotation vector can be expressed as

$$\mathbf{\Omega} = \Omega \cos\left(\varphi\right)\mathbf{j} + \Omega\sin\left(\varphi\right)\mathbf{k} \ ,$$

where Ω is the angular velocity and φ is the latitude. Equation (1.2) is called *the equation of motion* [Gill, 1982].

In component form the equations become

$$x: \qquad \rho\left(\frac{Du}{Dt} + f_*w - fv\right) = -\frac{\partial p}{\partial x} + \frac{\partial \tau^{xx}}{\partial x} + \frac{\partial \tau^{xy}}{\partial y} + \frac{\partial \tau^{xz}}{\partial z} \ ,$$

$$y: \qquad \rho\left(\frac{Dv}{Dt} + fu\right) = -\frac{\partial p}{\partial y} + \frac{\partial \tau^{xy}}{\partial x} + \frac{\partial \tau^{yy}}{\partial y} + \frac{\partial \tau^{yz}}{\partial z} \ ,$$

$$z: \qquad \rho\left(\frac{Dw}{Dt} - f_*u\right) = -\frac{\partial p}{\partial z} - \rho g + \frac{\partial \tau^{xz}}{\partial x} + \frac{\partial \tau^{yz}}{\partial y} + \frac{\partial \tau^{zz}}{\partial z} \ ,$$

where

$$f = 2\Omega\sin\left(\varphi\right)$$

is the Coriolis parameter,

$$f_* = 2\Omega\cos\left(\varphi\right)$$

is the reciprocal Coriolis parameter, and τ is the stress tensor [Cushman-Roisin, 1994].

A Cartesian coordinate system where the positive x, y and z-axis point to the east, north and upwards, respectively, is used. The reference level is at $z = 0$, where the water is at equilibrium, $z = -H(x,y)$ is the bottom topography, and the free surface is located at $z = \eta\left(x,y,t\right)$.

1.2 Approximations

Following Blumberg and Mellor [1987], two approximations will be applied in order to simplify the equations. First, it will be assumed that the density can be split into a mean value ρ_0 and a small perturbation. Then all density differences that are not multiplied by gravity can be neglected, *the Boussinesq approximation*. Next, it will be assumed that the pressure at a given depth equals the weight of the water above, *the hydrostatic approximation*.

The equation of continuity becomes

$$\nabla \cdot \mathbf{V} = 0$$

which is equivalent to assuming that the fluid is incompressible [Gill, 1982]. In other words, conservation of mass can now be considered to be conservation of volume.

The reciprocal Coriolis parameter is generally very small, and can be set to zero. In the following, only cases where the variation of the Coriolis force with latitude is negligible will be considered, so f will be taken as a constant. That is, all events will take place on a *f-plane* [Cushman-Roisin, 1994].

Often, it is sufficient to study the statistically averaged flow, leaving aside all turbulence fluctuations. Reynolds suggested to divide each variable into a mean and a fluctuation, e.g. $\mathbf{V} = \overline{\mathbf{V}} + \mathbf{V}_f$ [Pond and Pickard, 1983]. The mean part is found by averaging the value over a time period. Since only mean values are used from now on, bars are dropped.

The Reynolds averaged momentum equations [Blumberg and Mellor, 1987] become

$$
\begin{aligned}
\frac{\partial u}{\partial t} + \mathbf{V} \cdot \nabla u - fv &= -\frac{1}{\rho_0}\frac{\partial p}{\partial x} + F_x \ , \\
\frac{\partial v}{\partial t} + \mathbf{V} \cdot \nabla v + fu &= -\frac{1}{\rho_0}\frac{\partial p}{\partial y} + F_y \ , \\
\rho g &= -\frac{\partial p}{\partial z} \ ,
\end{aligned}
$$

The vertical viscosity is set to zero. F_x and F_y represent the small-scale unresolved processes according to

$$
F_x = \frac{\partial}{\partial x}\left[2A_M\frac{\partial u}{\partial x}\right] + \frac{\partial}{\partial y}\left[A_M\left(\frac{\partial u}{\partial y} + \frac{\partial v}{\partial x}\right)\right] \ , \tag{1.3}
$$

and

$$
F_y = \frac{\partial}{\partial y}\left[2A_M\frac{\partial v}{\partial y}\right] + \frac{\partial}{\partial x}\left[A_M\left(\frac{\partial u}{\partial y} + \frac{\partial v}{\partial x}\right)\right] \ . \tag{1.4}
$$

A_M is the horizontal viscosity coefficient.

The energy equation becomes

$$
\frac{D\rho}{Dt} = 0 \ ,
$$

where the diffusivities are set to zero.

1.3   The linearised equations

In this study, the linearised version of the stated governing equations will be solved, as in Mellor et al. [1998]. The equation of continuity is unchanged

$$\frac{\partial u}{\partial x} + \frac{\partial v}{\partial y} + \frac{\partial w}{\partial z} = 0 \ .$$

To yet again simplify the equations, the density field can be split into a reference density $\rho_{ref}(z)$ and a perturbation density $\rho'(x, y, z, t)$ according to

$$\rho(x, y, z, t) = \rho_{ref}(z) + \rho'(x, y, z, t) \ .$$

The equations become

$$\frac{\partial u}{\partial t} - fv = -\frac{1}{\rho_0}\frac{\partial p}{\partial x} + F_x \ , \tag{1.5}$$

$$\frac{\partial v}{\partial t} + fu = -\frac{1}{\rho_0}\frac{\partial p}{\partial y} + F_y \ , \tag{1.6}$$

$$\rho g = -\frac{\partial p}{\partial z} \ , \tag{1.7}$$

$$\frac{\partial \rho'}{\partial t} + w\frac{d\rho_{ref}}{dz} = 0 \ , \tag{1.8}$$

where F_x and F_y are given by (1.3) and (1.4).

By integrating (1.7) from z to the free surface η, the pressure at depth z can be found. The total pressure may be described as

$$p(x, y, z, t) = p_{atm} + p_\eta(x, y, t) + p_{int}(x, y, z, t) \ .$$

Here p_{atm} is the constant atmospheric pressure, $p_\eta = g\rho_0\eta$ is the pressure from the surface elevation and $p_{int} = g\int_z^0 \rho(x, y, z', t)dz'$ is the internal pressure.

To reduce the local errors, the reference stratification ρ_{ref} is subtracted from the density ρ in the computations of p_{int}. The internal pressure used in the POM calculation is therefore

$$p_{int} = g\int_z^0 \rho'(x, y, z', t)dz' \ .$$

Since the following discussion will concern the internal pressure gradient, the perturbation ρ' will be used exclusively in the equations. From this point, ρ will be written instead of ρ'.

Mode splitting

An ocean model should be able to reproduce different physical phenomena. To reduce the computational cost of for instance resolving fast moving external gravity waves together with slow moving internal gravity waves, the model is split into two different modes. In the POM the external mode calculates the vertically integrated equations with small time steps, while the internal mode calculates the full equations with longer time steps [Mellor, 2003].

1.4   Transformation to σ-coordinates

The σ-coordinate models are terrain-following, which means that the vertical layers are shaped after the topography, see Figure 3.

Therefore, a transformation from (x, y, z, t) to (x^*, y^*, σ, t^*) coordinates is needed

$$x^* = x \qquad y^* = y \qquad \sigma = \frac{z - \eta}{H + \eta} \qquad t^* = t \ .$$

Note that $\sigma = 0$ at $z = \eta$ and $\sigma = -1$ at $z = -H$.

Let $D \equiv H + \eta$ and apply the chain rule to obtain

$$\frac{\partial G}{\partial x} = \frac{\partial G}{\partial x^*} - \frac{\partial G}{\partial \sigma} \left(\frac{\sigma}{D} \frac{\partial D}{\partial x^*} + \frac{1}{D} \frac{\partial \eta}{\partial x^*} \right),$$

$$\frac{\partial G}{\partial y} = \frac{\partial G}{\partial y^*} - \frac{\partial G}{\partial \sigma} \left(\frac{\sigma}{D} \frac{\partial D}{\partial y^*} + \frac{1}{D} \frac{\partial \eta}{\partial y^*} \right),$$

$$\frac{\partial G}{\partial z} = \frac{1}{D} \frac{\partial G}{\partial \sigma} \ ,$$

$$\frac{\partial G}{\partial t} = \frac{\partial G}{\partial t^*} - \frac{\partial G}{\partial \sigma} \left(\frac{\sigma}{D} \frac{\partial D}{\partial t^*} + \frac{1}{D} \frac{\partial \eta}{\partial t^*} \right),$$

where G is an arbitrary field variable.

By using the transformation formulae above, the following expression for the partial derivative of the pressure that appears in (1.5) is obtained

$$\frac{\partial p}{\partial x} = g \int_z^\eta \frac{\partial \rho}{\partial x} dz = gD \int_\sigma^0 \frac{\partial \rho}{\partial x^*} - \frac{\partial \rho}{\partial \sigma} \left(\frac{\sigma}{D} \frac{\partial D}{\partial x^*} + \frac{1}{D} \frac{\partial \eta}{\partial x^*} \right) d\sigma \ .$$

A similar expression for the pressure term in (1.6) can be found. The internal pressure gradient (here represented by the x-component) is

$$\frac{\partial p_{int}}{\partial x} = gD \int_\sigma^0 \left(\frac{\partial \rho}{\partial x^*} - \frac{\sigma}{D} \frac{\partial \rho}{\partial \sigma} \frac{\partial D}{\partial x^*} \right) d\sigma \ . \tag{1.9}$$

Equation (1.9) holds the source of the internal pressure gradient error. Horizontal pressure gradients are usually small, since the largest density changes often appear in the vertical. However, near steep topography, the horizontal pressure gradient in σ-coordinates along the tilting surfaces of constant σ will be large due to the vertical changes [Slørdal, 1997]. The truncation errors in the possibly large terms in (1.9) can be quite severe.

By using integration by parts, it is possible to rewrite the last term of the integrand in (1.9) according to

$$\int_\sigma^0 \sigma \frac{\partial \rho}{\partial \sigma} d\sigma = -\sigma\rho - \int_\sigma^0 \rho \, d\sigma \; .$$

Then (1.9) becomes

$$\frac{\partial p_{int}}{\partial x} = g \int_\sigma^0 \left(D \frac{\partial \rho}{\partial x^*} + \frac{\partial D}{\partial x^*} \rho \right) d\sigma + g\sigma\rho \frac{\partial D}{\partial x^*} \; . \tag{1.10}$$

Observe that the integrand in (1.10) does no longer contain a derivative with respect to σ. It is slightly less complicated to discretise, and gives approximately the same numerical results as the discretisations based on (1.9) [Berntsen and Oey, 2010]. The computations in this study are mainly based on (1.10), although some experiments will also be performed using (1.9).

From this point, all asterisks are dropped.

Chapter 2

The finite volume approach

2.1 Discretising in the POM

The C-grid

The Princeton Ocean Model [Blumberg and Mellor, 1987] uses the staggered Arakawa C-grid. The value of the dynamic depth D, and the density ρ, is given in the middle of the cell. The velocity component in the x-direction, u, is given to the west of the ρ-point. The velocity component in the y-direction, v, is given to the south, see Figure 2.1 for the horizontal view.
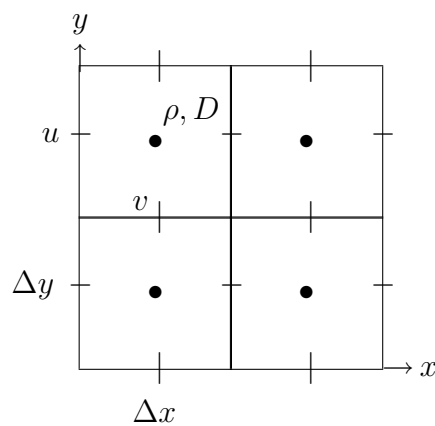

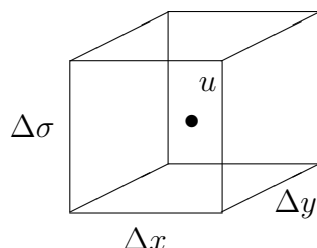**Figure 2.1:** The Arakawa C-grid, horizontal view.

Figure 2.2: The three-dimensional cell.

The internal pressure computation

Since the case considered is three-dimensional, the model domain is discretised into a finite number of fixed control volumes. For the computation of the internal pressure gradient, the three-dimensional grid cell is centred around the u-point for the x-component (see Figure 2.2), and the v-point for the y-component. In the standard POM-code, the pressure forces are assumed to be constant in each cell, therefore only the value of the gradient in the middle of the cell is calculated.

As an example, consider the internal pressure gradient in the x-direction, which is derived from the one-dimensional integral in equation (1.9). The trapezoidal rule is used for the vertical integration, and the value of the integrand is computed in each u-point, using central differences for all spatial derivatives.

2.2   A new integral

It is possible to estimate the pressure forces over finite volumes instead. While finite differences approximate the value of a function in a point, the finite volume approach approximate the average value of a function over an interval, or a volume. The two are closely related, and one approach can often be interpreted as the other [LeVeque, 2002].

In the finite volume approach, the average value of the integrand over the three-dimensional cell will be estimated. By evaluating an integral in
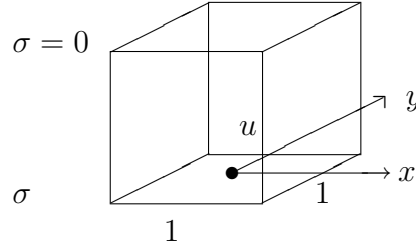
Figure 2.3: The domain of integration in the finite volume approach, see equation (2.1).

three dimensions, the pressure differences that can occur on different sides of the grid cell will be taken into account. Hopefully, this will result in a more accurate computation.

From this point, the focus will be on the x-component of the internal pressure gradient. Using equation (1.10), the new expression for the internal pressure in the x-direction (henceforth omitting the subscript) becomes

$$\frac{\partial p}{\partial x} = \left[g \int_{-\frac{1}{2}}^{\frac{1}{2}} \int_{-\frac{1}{2}}^{\frac{1}{2}} \left[\int_{\sigma}^{0} \left(D \frac{\partial \rho}{\partial x} + \frac{\partial D}{\partial x} \rho \right) d\sigma + \sigma \rho \frac{\partial D}{\partial x} \right] dx dy \right] . \qquad (2.1)$$

Here, the horizontal part of the cells are scaled to have the area 1. The domain of integration is displayed in Figure 2.3.

The discussion below will concern the horizontal integration, as earlier studies indicate that this computation is the most significant for the error, see [Berntsen and Oey, 2010]. The trapezoidal rule will always be used in the vertical.

2.3   Evaluating the new integral

By using appropriate weights when computing $\frac{\partial \rho}{\partial x}$, $\frac{\partial D}{\partial x}$, ρ, and D in u-points, a numerical method of integration for the horizontal part of equation (2.1) can be constructed. That is, the integral

$$\int_{-\frac{1}{2}}^{\frac{1}{2}} \int_{-\frac{1}{2}}^{\frac{1}{2}} \left[\left(D\frac{\partial \rho}{\partial x} + \frac{\partial D}{\partial x}\rho \right) + \sigma\rho\frac{\partial D}{\partial x} \right] dxdy \ , \qquad (2.2)$$

will be considered.

One can estimate the integral by multiplying the value of the integrand with the area of the cell, which is 1 after the scaling. The weights can be found by first making an approximation of the integrand, and then demand that the method is exact for polynomials up to a certain order by calculating the exact value of the integral in the given case. This is *the method of undetermined coefficients.*

The translation of the coordinate system to the centre of each cell is helpful, because it leads to a symmetrical area of integration. Therefore, the integral of any polynomial of odd order over this region will be zero, and a centred method of numerical integration will automatically satisfy the demands of exactness.

Polynomials of even order will provide a system of equations to be solved. First, the simplest possible case will be addressed.

2.3.1   Method A: Standard 2nd order POM

Let only two ρ or D-points be included when estimating $\frac{\partial \rho}{\partial x}$, $\frac{\partial D}{\partial x}$, ρ and D in a u-point. The points are labelled with their x and y coordinates. Note that the u-point now lies in the origin of the horizontal coordinate system. For example, the point $\rho_{\frac{1}{2},0}$ is placed on the x-axis at a distance $\frac{1}{2}$ to the east of the u-point, see Figure 2.4.

For D and $\frac{\partial \rho}{\partial x}$ in a u-point, the equations become

$$D|_u = \alpha(D_{\frac{1}{2},0} + D_{-\frac{1}{2},0}) \ , \qquad (2.3)$$

$$\frac{\partial \rho}{\partial x}|_u = a(\rho_{\frac{1}{2},0} - \rho_{-\frac{1}{2},0}) \ .$$

This represents an interpolation of the D-values, and a basic central finite difference approach to the $\frac{\partial \rho}{\partial x}$-term. The fixed weights defining the integration rule are given by α and a.

The two points will make it possible to find a method that is exact for $D = 1$ and $\frac{\partial \rho}{\partial x} = 1$. In this case, the exact value of the integral is

$$\int_{-\frac{1}{2}}^{\frac{1}{2}} \int_{-\frac{1}{2}}^{\frac{1}{2}} D\frac{\partial \rho}{\partial x} \ dxdy = \int_{-\frac{1}{2}}^{\frac{1}{2}} \int_{-\frac{1}{2}}^{\frac{1}{2}} 1 \ dxdy = 1 \ . \qquad (2.4)$$
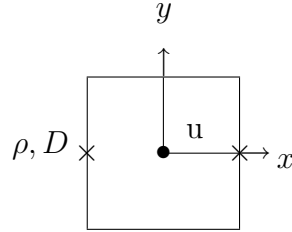
Figure 2.4: Points ρ, D ($\times$) and u ($\bullet$) at a σ-level used in the standard 2nd order POM method, Method A.

The numerical approximation of the integral of $D = 1$ and $\frac{\partial \rho}{\partial x} = 1$, using (2.3), is

$$\int_{-\frac{1}{2}}^{\frac{1}{2}} \int_{-\frac{1}{2}}^{\frac{1}{2}} \alpha \left(D_{\frac{1}{2},0} + D_{-\frac{1}{2},0} \right) \cdot a \left(\rho_{\frac{1}{2},0} - \rho_{-\frac{1}{2},0} \right) dxdy =$$

$$\int_{-\frac{1}{2}}^{\frac{1}{2}} \int_{-\frac{1}{2}}^{\frac{1}{2}} \alpha \cdot 2 \cdot a \cdot 1 \ dxdy = 1 \ ,$$

which leads to

$$\alpha a = \frac{1}{2} \ .$$

A possible solution is $\alpha = \frac{1}{2}$ and $a = 1$, which are the weights used in the standard POM-code. These are also the only weights that will make the approximation (2.3) *consistent*, this concept will be explained in a moment. The same rule will be applicable to the term $\rho \frac{\partial D}{\partial x} = 1$ from (2.1).

Applying a second order finite volume method will in this case correspond to using a finite difference approach, that is, it is equivalent to assuming a constant pressure force. It is clear that the 2nd order POM method can be interpreted as the simplest in a family of finite volume methods. It is desirable to follow this line of thought, and expand the standard 2nd order POM method by including new points. Increasing the order of the finite

volume method will hopefully reduce the error and result in a more robust model.

The calculation of the internal pressure gradient in the y-direction is similar to that of the x-direction. The stencil from Figure 2.4 is rotated 90 degrees, and the coordinate system is centred in a v-point.

Consistency

A numerical scheme is consistent if the truncation error of the discretisation goes to zero as the time step and the grid refinement approach zero [Haidvogel and Beckmann, 1999]. Taylor expansions of the displaced variables give us the discretised expressions for the derivative and the interpolated values. The derivative is equal to the second equation of (2.3) with $a = 1$, divided by the length between the displacements, plus higher order terms. In other words, the expression from (2.3) with $a = 1$ corresponds to the approximation of one derivative.

For a consistent approximation, the weights have to add up to exactly one derivative and one variable value in each point. Above, the weight $a = 1$ will produce one derivative, and the weight $\alpha = \frac{1}{2}$ will compute the average value of D or ρ from two points, and therefore scale it to the single value corresponding to the middle point.

2.3.2 Method B: Expanding in the y-direction

The standard 2nd order POM method includes only two ρ or D-points. Now, a 4th order method is sought. If two points are added symmetrically in the y-direction above and below the cell (see Figure 2.5), the following expressions for D and $\frac{\partial \rho}{\partial x}$ in a u-point are obtained

$$
\begin{aligned}
D|_u &= \alpha \sum D_{\pm\frac{1}{2},0} + \beta \sum D_{\pm\frac{1}{2},\pm1} \ , &(2.5)\\
\frac{\partial \rho}{\partial x}\Big|_u &= a\left(\rho_{\frac{1}{2},0} - \rho_{-\frac{1}{2},0}\right) + b\left[\left(\rho_{\frac{1}{2},1} - \rho_{-\frac{1}{2},1}\right) + \left(\rho_{\frac{1}{2},-1} - \rho_{-\frac{1}{2},-1}\right)\right] \ .
\end{aligned}
$$

Here, the fixed weights β and b are needed in addition to α and a.

The summation is done according to

$$
\sum D_{\pm\frac{1}{2},\pm1} = D_{\frac{1}{2},1} + D_{-\frac{1}{2},1} + D_{\frac{1}{2},-1} + D_{-\frac{1}{2},-1} \ .
$$

If it is demanded that the rule is exact for $D = 1$ and $\frac{\partial \rho}{\partial x} = 1$, remembering (2.4), the approximation becomes
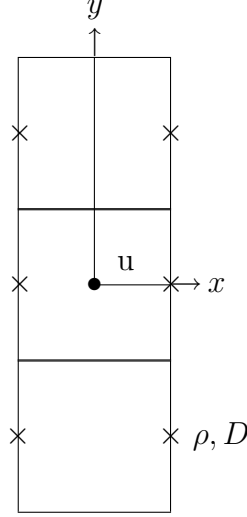
Figure 2.5: Points ρ, D ($\times$) and u ($\bullet$) at a σ-level used to construct the Method B.

$$\int_{-\frac{1}{2}}^{\frac{1}{2}} \int_{-\frac{1}{2}}^{\frac{1}{2}} D\frac{\partial\rho}{\partial x}\ dxdy\ = \tag{2.6}$$

$$\int_{-\frac{1}{2}}^{\frac{1}{2}} \int_{-\frac{1}{2}}^{\frac{1}{2}} (2\alpha + 4\beta) \cdot (a + 2b)\ dxdy\ =\ 1\ ,$$

leading to

$$(2\alpha + 4\beta) \cdot (a + 2b)\ =\ 1\ . \tag{2.7}$$

So as to exploit the new set of points, it is required that the method should also be exact for $D = x^2$ (while $\frac{\partial\rho}{\partial x} = 1$ as before). The exact value of the integral becomes

$$\int_{-\frac{1}{2}}^{\frac{1}{2}} \int_{-\frac{1}{2}}^{\frac{1}{2}} D\frac{\partial\rho}{\partial x}\ dxdy = \int_{-\frac{1}{2}}^{\frac{1}{2}} \int_{-\frac{1}{2}}^{\frac{1}{2}} x^2\ dxdy = \frac{1}{12}\ . \tag{2.8}$$

After the substitution of the values of D and ρ at the chosen points in (2.5), the equations become

$$\int_{-\frac{1}{2}}^{\frac{1}{2}} \int_{-\frac{1}{2}}^{\frac{1}{2}} D\frac{\partial \rho}{\partial x} \ dxdy \ = $$

$$\int_{-\frac{1}{2}}^{\frac{1}{2}} \int_{-\frac{1}{2}}^{\frac{1}{2}} \left(\frac{1}{2}\alpha + \beta\right) \cdot (a + 2b) \ dxdy \ = \ \frac{1}{12} \ ,$$

which leads to

$$\left(\frac{1}{2}\alpha + \beta\right) \cdot (a + 2b) = \frac{1}{12} \ . \tag{2.9}$$

Rewriting (2.7) gives

$$\left(\frac{1}{2}\alpha + \beta\right) \cdot (a + 2b) = \frac{1}{4} \ . \tag{2.10}$$

It is easy to see that the equations (2.9) and (2.10) can not be fulfilled at the same time. Therefore, the approach applied here will not lead to a new, 4th order method of integration. The same will be true for the term $\rho\frac{\partial D}{\partial x} = 1$ from (2.1).

However, a new 2nd order method can be found by using these points. This will be addressed in Chapter 3.

2.3.3 Method C: Two more points in the horizontal

Now, ignore the new points from the previous section. Instead, include one additional point on each side in the x-direction, according to

$$D|_u \ = \ \alpha \sum D_{\pm\frac{1}{2},0} + \gamma \sum D_{\pm\frac{3}{2},0} \tag{2.11}$$

$$\frac{\partial \rho}{\partial x}|_u \ = \ a\left(\rho_{\frac{1}{2},0} - \rho_{-\frac{1}{2},0}\right) + c\left(\rho_{\frac{3}{2},0} - \rho_{-\frac{3}{2},0}\right) \ ,$$

see Figure 2.6. The constants γ and c are the fixed weights needed in the new approximation.

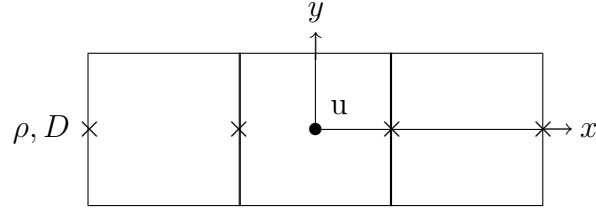Demanding that the method should be exact for $D = 1, x^2$ while $\frac{\partial \rho}{\partial x} = 1$ leads to

Figure 2.6: Points ρ, D ($\times$) and u ($\bullet$) at a σ-level used to construct the Method C.

$$\int_{-\frac{1}{2}}^{\frac{1}{2}} \int_{-\frac{1}{2}}^{\frac{1}{2}} D\frac{\partial \rho}{\partial x} \; dxdy \;\; =$$

$$\int_{-\frac{1}{2}}^{\frac{1}{2}} \int_{-\frac{1}{2}}^{\frac{1}{2}} (2\alpha + 2\gamma) \cdot (a + 3c) \; dxdy \;\; = \;\; 1 \; ,$$

and

$$\int_{-\frac{1}{2}}^{\frac{1}{2}} \int_{-\frac{1}{2}}^{\frac{1}{2}} D\frac{\partial \rho}{\partial x} \; dxdy \;\; =$$

$$\int_{-\frac{1}{2}}^{\frac{1}{2}} \int_{-\frac{1}{2}}^{\frac{1}{2}} \left(\frac{1}{2}\alpha + \frac{9}{2}\gamma\right) \cdot (a + 3c) \; dxdy \;\; = \;\; \frac{1}{12} \; .$$

For consistency,

$$a + 3c \;\; = \;\; 1$$

is needed. This leads to

$$2\alpha + 2\gamma \;\; = \;\; 1$$
$$\frac{1}{2}\alpha + \frac{9}{2}\gamma \;\; = \;\; \frac{1}{12} \; .$$

Correspondingly, requiring $\frac{\partial \rho}{\partial x} = 1, x^2$ while $D = 1$, gives

$$\int_{-\frac{1}{2}}^{\frac{1}{2}} \int_{-\frac{1}{2}}^{\frac{1}{2}} D\frac{\partial \rho}{\partial x} \, dxdy \quad =$$

$$\int_{-\frac{1}{2}}^{\frac{1}{2}} \int_{-\frac{1}{2}}^{\frac{1}{2}} (a + 3c) \cdot (2\alpha + 2\gamma) \quad = \quad 1 \ .$$

and

$$\int_{-\frac{1}{2}}^{\frac{1}{2}} \int_{-\frac{1}{2}}^{\frac{1}{2}} D\frac{\partial \rho}{\partial x} \, dxdy \quad =$$

$$\int_{-\frac{1}{2}}^{\frac{1}{2}} \int_{-\frac{1}{2}}^{\frac{1}{2}} \left(\frac{1}{12}a + \frac{27}{12}c \right) \cdot (2\alpha + 2\gamma) \ dxdy \quad = \quad \frac{1}{12} \ .$$

Substituting

$$2\alpha + 2\gamma \quad = \quad 1 \ ,$$

leads to

$$a + 3c \quad = \quad 1$$
$$a + 27c \quad = \quad 1 \ .$$

The system of equations can only be solved if $c = 0$. This results in the following set of weights

$$\alpha = \frac{13}{24} \ , \ \gamma = -\frac{1}{24} \ , \ a = 1 \ , \ \text{and } c = 0 \ . \tag{2.12}$$

Consequently, the information from the points that are furthest away from the origin is not used for the computation of the derivative.

The stencil in Figure 2.6 is identical to the one used for constructing the 4th order McCalpin-method [McCalpin, 1994]. The McCalpin method is found by doing Taylor expansions around the middle point to approximate the derivative. It is important to note that the method obtained by McCalpin is not equal to the finite volume method developed in this text. Also observe that the order of the method is decided for the integral of the *product*, not the individual terms.
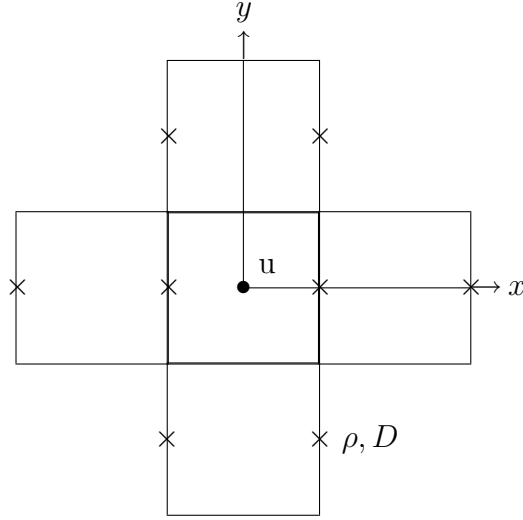
Figure 2.7: Points ρ, D ($\times$) and u ($\bullet$) at a σ-level used to construct the Method D.

2.3.4 Method D: Six new points

Yet another method can be constructed by utilising the information in all of the six points previously discussed, see Figure 2.7.

Consider the following approximation

$$
\begin{aligned}
D|_u &= \alpha \sum D_{\pm\frac{1}{2},0} + \beta \sum D_{\pm\frac{1}{2},\pm1} + \gamma \sum D_{\pm\frac{3}{2},0} \;, \\
\frac{\partial \rho}{\partial x}\bigg|_u &= a\left(\rho_{\frac{1}{2},0} - \rho_{-\frac{1}{2},0}\right) \\
&\quad + b\left[\left(\rho_{\frac{1}{2},1} - \rho_{-\frac{1}{2},1}\right) + \left(\rho_{\frac{1}{2},-1} - \rho_{-\frac{1}{2},-1}\right)\right] \\
&\quad + c\left(\rho_{\frac{3}{2},0} - \rho_{-\frac{3}{2},0}\right) \;.
\end{aligned}
\tag{2.13}
$$

In addition,

$$
\int_{-\frac{1}{2}}^{\frac{1}{2}} \int_{-\frac{1}{2}}^{\frac{1}{2}} y^2 \; dx dy = \frac{1}{12} \;,
\tag{2.14}
$$

will be used together with (2.4) and (2.8). If the method has to be exact for $D = 1, x^2, y^2$, while $\frac{\partial \rho}{\partial x} = 1$, (2.13) leads to

$$\int_{-\frac{1}{2}}^{\frac{1}{2}} \int_{-\frac{1}{2}}^{\frac{1}{2}} D\frac{\partial \rho}{\partial x} \ dxdy \ = $$

$$\int_{-\frac{1}{2}}^{\frac{1}{2}} \int_{-\frac{1}{2}}^{\frac{1}{2}} (2\alpha + 4\beta + 2\gamma) \cdot (a + 2b + 3c) \ dxdy \ = \ 1 \ ,$$

and

$$\int_{-\frac{1}{2}}^{\frac{1}{2}} \int_{-\frac{1}{2}}^{\frac{1}{2}} D\frac{\partial \rho}{\partial x} \ dxdy \ = $$

$$\int_{-\frac{1}{2}}^{\frac{1}{2}} \int_{-\frac{1}{2}}^{\frac{1}{2}} \left(\frac{1}{2}\alpha + \beta + \frac{9}{2}\gamma \right) \cdot (a + 2b + 3c) \ dxdy \ = \ \frac{1}{12} \ ,$$

together with

$$\int_{-\frac{1}{2}}^{\frac{1}{2}} \int_{-\frac{1}{2}}^{\frac{1}{2}} D\frac{\partial \rho}{\partial x} \ dxdy \ = $$

$$\int_{-\frac{1}{2}}^{\frac{1}{2}} \int_{-\frac{1}{2}}^{\frac{1}{2}} (4\beta) \cdot (a + 2b + 3c) \ dxdy \ = \ \frac{1}{12} \ .$$

On substituting

$$a + 2b + 3c \ = \ 1 \ ,$$

needed for consistency, the system of equations becomes

$$2\alpha + 4\beta + 2\gamma \ = \ 1 \ ,$$
$$\frac{1}{2}\alpha + \beta + \frac{9}{2}\gamma \ = \ \frac{1}{12} \ ,$$
$$4\beta \ = \ \frac{1}{12} \ .$$

To determine the rest of the weights, exactness for $\frac{\partial \rho}{\partial x} = 1, x^2, y^2$ and $D = 1$ is demanded. This leads to

$$\int_{-\frac{1}{2}}^{\frac{1}{2}} \int_{-\frac{1}{2}}^{\frac{1}{2}} D \frac{\partial \rho}{\partial x} \ dxdy \ =$$

$$\int_{-\frac{1}{2}}^{\frac{1}{2}} \int_{-\frac{1}{2}}^{\frac{1}{2}} (a + 2b + 3c) \cdot (2\alpha + 4\beta + 2\gamma) \ = \ 1 \ ,$$

and

$$\int_{-\frac{1}{2}}^{\frac{1}{2}} \int_{-\frac{1}{2}}^{\frac{1}{2}} D \frac{\partial \rho}{\partial x} \ dxdy \ =$$

$$\int_{-\frac{1}{2}}^{\frac{1}{2}} \int_{-\frac{1}{2}}^{\frac{1}{2}} \left(\frac{1}{12}a + \frac{1}{6}b + \frac{27}{12}c \right) \cdot (2\alpha + 4\beta + 2\gamma) \ dxdy \ = \ \frac{1}{12} \ ,$$

together with

$$\int_{-\frac{1}{2}}^{\frac{1}{2}} \int_{-\frac{1}{2}}^{\frac{1}{2}} D \frac{\partial \rho}{\partial x} \ dxdy \ =$$

$$\int_{-\frac{1}{2}}^{\frac{1}{2}} \int_{-\frac{1}{2}}^{\frac{1}{2}} (2b) \cdot (2\alpha + 4\beta + 2\gamma) \ dxdy \ = \ \frac{1}{12} \ .$$

The system of equations becomes

$$a + 2b + 3c \ = \ 1 \ ,$$
$$a + 2b + 27c \ = \ 1 \ ,$$
$$2b \ = \ \frac{1}{12} \ .$$

This system can only be solved exactly if $c = 0$. The following set of weights is obtained

$$\alpha = \frac{1}{2} \ , \ \beta = \frac{1}{48} \ , \ \gamma = -\frac{1}{24} \ , \ a = \frac{11}{12} \ , \ b = \frac{1}{24} \ , \ \text{and} \ c = 0 \ .$$

Again, the same method applies for the integral of $\rho \frac{\partial D}{\partial x}$. All of the above methods can also be used to compute the y-component of the pressure.
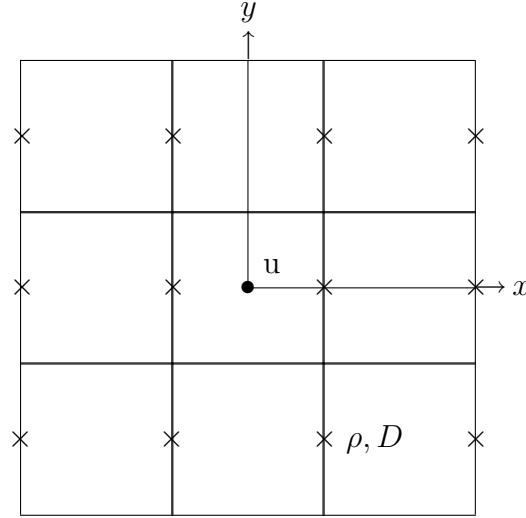
Figure 2.8: Points ρ, D ($\times$) and u ($\bullet$) at a σ-level used to construct the Method E.

2.3.5 Method E: Ten points - The last expansion

The approach can be taken one step further by adding four more points to the scheme, see Figure 2.8.

Now, the approximation becomes

$$
\begin{aligned}
D|_u &= \alpha \sum D_{\pm\frac{1}{2},0} + \beta \sum D_{\pm\frac{1}{2},\pm 1} + \gamma \sum D_{\pm\frac{3}{2},0} + \delta \sum D_{\pm\frac{3}{2},\pm 1} \\
\frac{\partial \rho}{\partial x}\Big|_u &= a\left(\rho_{\frac{1}{2},0} - \rho_{-\frac{1}{2},0}\right) + \\
&\quad b\left[\left(\rho_{\frac{1}{2},1} - \rho_{-\frac{1}{2},1}\right) + \left(\rho_{\frac{1}{2},-1} - \rho_{-\frac{1}{2},-1}\right)\right] + \\
&\quad c\left(\rho_{\frac{3}{2},0} - \rho_{-\frac{3}{2},0}\right) + \\
&\quad d\left[\left(\rho_{\frac{3}{2},1} - \rho_{-\frac{3}{2},1}\right) + \left(\rho_{\frac{3}{2},-1} - \rho_{-\frac{3}{2},-1}\right)\right] .
\end{aligned}
\tag{2.15}
$$

The following integral will be useful

$$
\int_{-\frac{1}{2}}^{\frac{1}{2}} \int_{-\frac{1}{2}}^{\frac{1}{2}} x^4 \, dx dy = \frac{1}{80} \ ,
$$

together with equations (2.4), (2.8), and (2.14). The hope is, again, to produce a more exact rule. In this case, a 6th order method is sought.

Exactness for $D = 1, x^2, y^2, x^4$, while $\frac{\partial \rho}{\partial x} = 1$, is demanded. Equations (2.15) give

$$\int_{-\frac{1}{2}}^{\frac{1}{2}} \int_{-\frac{1}{2}}^{\frac{1}{2}} D\frac{\partial \rho}{\partial x} \, dxdy \quad = \quad \text{(2.16)}$$

$$\int_{-\frac{1}{2}}^{\frac{1}{2}} \int_{-\frac{1}{2}}^{\frac{1}{2}} (2\alpha + 4\beta + 2\gamma + 4\delta) \cdot (a + 2b + 3c + 6d) \quad = \quad 1 \ ,$$

and

$$\int_{-\frac{1}{2}}^{\frac{1}{2}} \int_{-\frac{1}{2}}^{\frac{1}{2}} D\frac{\partial \rho}{\partial x} \, dxdy \quad = \quad \text{(2.17)}$$

$$\int_{-\frac{1}{2}}^{\frac{1}{2}} \int_{-\frac{1}{2}}^{\frac{1}{2}} \left(\frac{1}{2}\alpha + \beta + \frac{9}{2}\gamma + 9\delta\right) \cdot (a + 2b + 3c + 6d) \ dxdy \quad = \quad \frac{1}{12} \ ,$$

together with

$$\int_{-\frac{1}{2}}^{\frac{1}{2}} \int_{-\frac{1}{2}}^{\frac{1}{2}} D\frac{\partial \rho}{\partial x} \, dxdy \quad = $$

$$\int_{-\frac{1}{2}}^{\frac{1}{2}} \int_{-\frac{1}{2}}^{\frac{1}{2}} (4\beta + 4\gamma) \cdot (a + 2b + 3c + 6d) \ dxdy \quad = \quad \frac{1}{12} \ ,$$

and

$$\int_{-\frac{1}{2}}^{\frac{1}{2}} \int_{-\frac{1}{2}}^{\frac{1}{2}} D\frac{\partial \rho}{\partial x} \, dxdy \quad = $$

$$\int_{-\frac{1}{2}}^{\frac{1}{2}} \int_{-\frac{1}{2}}^{\frac{1}{2}} \left(\frac{1}{8}\alpha + \frac{1}{4}\beta + \frac{81}{8}\gamma + \frac{81}{4}\delta\right) \cdot (a + 2b + 3c + 6d) \ dxdy \quad = \quad \frac{1}{80} \ .$$

Substitution of

$$(a + 2b + 3c + 6d) = 1 \ ,$$

needed for the consistency of the derivative, leads to

$$
\begin{aligned}
2\alpha + 4\beta + 2\gamma + 4\delta &= 1 \; , \\
\frac{1}{2}\alpha + \beta + \frac{9}{2}\gamma + 9\delta &= \frac{1}{12} \; , \\
4\beta + 4\delta &= \frac{1}{12} \; , \\
\frac{1}{8}\alpha + \frac{1}{4}\beta + \frac{81}{8}\gamma + \frac{81}{4}\delta &= \frac{1}{80} \; .
\end{aligned}
$$

Unfortunately, it is not possible to solve this system of equations exactly. At this point, the result should not be a surprise. The last expansion in this way, from Method A to Method B, led to the same problem. The points used can not lead to a new 6th order method.

2.3.6   When is the order increased?

The reason for the problem is quite simple. The methods A and C are one-dimensional, and therefore the desired increased order is obtained by expanding the stencil in only one direction. However, when it is attempted to go to 4th order in Method B, it is not possible to get the desired order in the x-direction. The approach fails. The same thing happens in Method E.

Method D is successful because it allows 4th order in both directions. This suggests that adding more points symmetrically on each side of the area in Figure 2.8 will eventually take the approach to 6th order. This will not be addressed further.

2.4   Comments on the methods

2.4.1   An inaccuracy

Note that this family of methods can not handle the case where both $\frac{\partial \rho}{\partial x}$ and D are assumed to be odd polynomials, e.g. $\frac{\partial \rho}{\partial x} = x$ and $D = x$. The product of the two will be x^2, and the exact value of this integral is $\frac{1}{12}$ from (2.8). With (2.11) and (2.13), the approximated integral value will just be zero. So in this case, the methods are quite inaccurate.

In other words, even though the approach gives enough equations to find the weights, it can not take all demands into consideration. This results in methods that are not truly of the order they were constructed to be.

2.4.2 Masking out land cells

For a test case with a realistic topography, there will be some cells where the depth is zero (islands, boundaries etc.). If this happens for any of the cells in the 2nd order POM method, a mask variable will ensure that the internal pressure gradient is set to zero. However, if this happens to any of the outlying cells in the Methods B, C, D and E, another mask variable will reduce the method to preserve the symmetry of the integration area. Method C will be reduced to the order of Method A, Method E will be reduced to Method C, or if necessary, even to Method A.

Chapter 3

A weighted approach

The points used in Methods A-E can provide a new set of approaches, inspired by the work of Thiem and Berntsen [2006].

3.1 More points, same order

3.1.1 An example

First, consider the stencil from Method B. By excluding the middle points (see Figure 3.1), a new 2nd order method can be found. If α and a are set to zero in equation (2.6), it becomes

$$\int_{-\frac{1}{2}}^{\frac{1}{2}} \int_{-\frac{1}{2}}^{\frac{1}{2}} D\frac{\partial \rho}{\partial x}\, dxdy \quad = \tag{3.1}$$

$$\int_{-\frac{1}{2}}^{\frac{1}{2}} \int_{-\frac{1}{2}}^{\frac{1}{2}} (4\beta)\cdot(2b)\, dxdy \quad = \quad 1\ , \tag{3.2}$$

which leads to

$$4\beta\cdot 2b \quad = \quad 1 \tag{3.3}$$

$$\beta b \quad = \quad \frac{1}{8}\ . \tag{3.4}$$

From the theory in the Chapter 2, it is clear that the consistent choice will be $\beta = \frac{1}{4}$ and $b = \frac{1}{2}$, and that the weights define a 2nd order finite volume method.
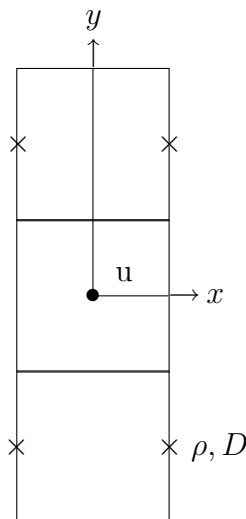
Figure 3.1: Points ρ, D ($\times$) and u ($\bullet$) at a σ-level used to construct the Method B, middle points excluded.

3.1.2   The motivation

Why is it desirable to include more points if it does not lead to higher order? Even though the approach from the previous example can only result in 2nd order accuracy, one can hope that the use of more points will increase the robustness, since information from a larger area is taken into consideration.

There is another possible advantage to extending the stencil. It tends to reduce the erroneous initial vorticity, and the vorticity error seems to be closely correlated to the long-term circulation [Marsaleix et al., 2009]. This error will be addressed in Chapter 5.

According to Thiem and Berntsen [2006], the internal pressure gradient error can be reduced by combining different approximations, and weight them against each other. In their work, the four points discussed above (Figure 3.1) were utilised to compute the internal pressure gradient in a grid that is rotated 45 degrees, see Figure 3.2. The idea was to find an optimal combination of the methods with weights that eliminated the largest of the numerical error terms. The rotated grid method was combined with the standard 2nd order POM method, and the two were weighted against each other with a fixed constant.

Thiem and Berntsen [2006] experienced that when only the rotated grid

method was used, the results became worse than for the standard POM method. However, by weighting the POM-approach three to four times more than the method from the rotated grid, more promising results were obtained.

In the following, this idea will be subject to further investigation. First of all, the theory from Chapter 2 will be used to show that the method from [Thiem and Berntsen, 2006] in fact can be interpreted as a 2nd order finite volume method.
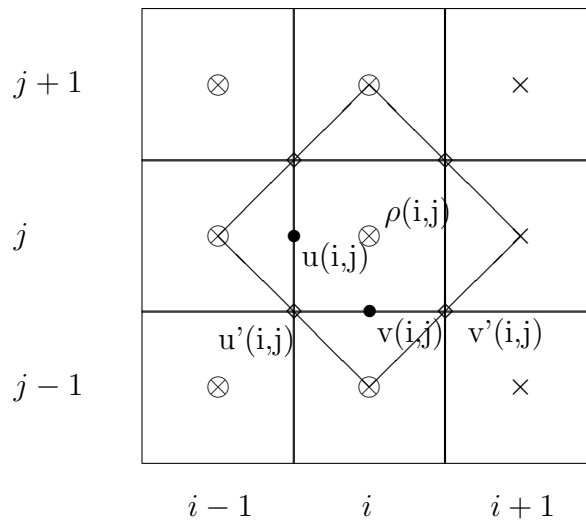

Figure 3.2: The rotated and original grid. The ρ-points are marked by ($\times$), ($\bullet$) are the u and v-points in the original grid, ($\diamond$) marks the u' and v'-points in the rotated grid, and ($\otimes$) are the points used in Method B.

3.2   The rotated grid method

In this section, $\frac{\partial \rho}{\partial x}\big|_u$ in a rotated grid will be found (Figure 3.2). The notation and step-by-step description of the calculation from [Thiem and Berntsen, 2006] will be used. The goal is to arrive at an expression for $\frac{\partial \rho}{\partial x}\big|_u$ that can be compared to the equations (2.5). The focus will still be on the x-component, in accordance with Chapter 2.

Recall that the calculation of the internal pressure gradient in the standard 2nd order POM would simply be based on

$$\delta_x \rho_{u(i,j)} \quad = \quad \rho(i,j) - \rho(i-1,j) \ .$$

where i and j are the discrete coordinates in the x- and y-direction, respectively. For the rotated grid, $\delta_{x'}\rho_{u'(i,j)}$ is computed in all $u'(i,j)$-points in the x'-direction according to

$$\delta_{x'}\rho_{u'(i,j)} = \rho(i,j) - \rho(i-1,j-1).$$

Then, $\delta_{y'}\rho_{u'(i,j)}$ is computed in all $u'(i,j)$-points in the y'-direction in a similar way

$$\delta_{y'}\rho_{u'(i,j)} = \rho(i-1,j) - \rho(i,j-1).$$

The same is done for the $v'(i,j)$-points.

$$\delta_{x'}\rho_{v'(i,j)} \quad = \quad \rho(i+1,j) - \rho(i,j-1)$$
$$\delta_{y'}\rho_{v'(i,j)} \quad = \quad \rho(i,j) - \rho(i+1,j-1) \ .$$

The components of the internal pressure gradients in u' and v'-points along the axes in the original grid are found. For the $u'(i,j)$-points in the x-direction, the component is given by

$$\begin{aligned}
\delta_x \rho_{u'(i,j)} \quad &= \quad \frac{\sqrt{2}}{2}\left(\delta_{x'}\rho_{u'(i,j)} - \delta_{y'}\rho_{u'(i,j)}\right) \\
&= \quad \frac{\sqrt{2}}{2}\left[\big(\rho(i,j) - \rho(i-1,j-1)\big) - \big(\rho(i-1,j) - \rho(i,j-1)\big)\right] \\
&= \quad \frac{\sqrt{2}}{2}\left[\big(\rho(i,j) - \rho(i-1,j)\big) + \big(\rho(i,j-1) - \rho(i-1,j-1)\big)\right] \ .
\end{aligned}$$

Similarly, for the $v'(i,j)$-points in the x-direction the following must be computed

$$\begin{aligned}
\delta_x \rho_{v'(i,j)} \quad &= \quad \frac{\sqrt{2}}{2}\left(\delta_{x'}\rho_{v'(i,j)} - \delta_{y'}\rho_{v'(i,j)}\right) \\
&= \quad \frac{\sqrt{2}}{2}\left[\big(\rho(i+1,j) - \rho(i,j-1)\big) - \big(\rho(i,j) - \rho(i+1,j-1)\big)\right] \\
&= \quad \frac{\sqrt{2}}{2}\left[\big(\rho(i+1,j) - \rho(i,j)\big) + \big(\rho(i+1,j-1) - \rho(i,j-1)\big)\right] \ .
\end{aligned}$$

The constant $\frac{\sqrt{2}}{2}$ comes from the transformation formula for vectors between coordinate systems that are rotated in proportion to each other, e.g. [Kundu and Cohen, 2004].

The internal pressure gradients from the u' and v'-points should then be interpolated to the u-points of the original grid according to

$$
\begin{aligned}
\delta_x \rho_{rot(i,j)} &= \frac{1}{2}\left(\delta_x \rho_{u'(i,j)} + \delta_x \rho_{v'(i,j+1)}\right) \\
&= \frac{1}{2\sqrt{2}}\Big[\rho(i,j) - \rho(i-1,j) + \rho(i,j-1) \ - \\
&\qquad \rho(i-1,j-1) + \rho(i,j) - \rho(i-1,j) \ + \\
&\qquad \rho(i,j+1) - \rho(i-1,j+1)\Big] \\
&= \frac{1}{2\sqrt{2}}\Big[2\rho(i,j) - 2\rho(i-1,j) + \rho(i,j-1) \ - \\
&\qquad \rho(i-1,j-1) + \rho(i,j+1) - \rho(i-1,j+1)\Big] \\
&= \frac{\sqrt{2}}{2}\Big[\rho(i,j) - \rho(i-1,j)\Big] \ + \\
&\qquad \frac{1}{2\sqrt{2}}\Big[\rho(i,j-1) - \rho(i-1,j-1) + \rho(i,j+1) - \rho(i-1,j+1)\Big] \ .
\end{aligned}
$$

The factor $\frac{1}{\sqrt{2}}$ is needed to scale the approximation because the grid length in the rotated grid is $\sqrt{2}$ times longer than in the original grid. If the last equation is divided by the scaling factor $\sqrt{2}$,

$$
\begin{aligned}
\frac{\partial \rho}{\partial x}\Big|_u &= \frac{1}{2}\big(\rho(i,j) - \rho(i-1,j)\big) + \\
&\quad \frac{1}{4}\big(\rho(i,j-1) - \rho(i-1,j-1) + \rho(i,j+1) - \rho(i-1,j+1)\big) \ ,
\end{aligned}
\tag{3.5}
$$

is obtained.

The approximation (3.5) is a combination of the 2nd order POM method of computing $\frac{\partial \rho}{\partial x}\big|_u$, and the method from Section 3.1.1, where the two approaches are weighted equally. A similar analysis will also give the weights for D and ρ in a u-point.

Now, consider the method in terms of the equations (2.5). The fixed weights are

$$\alpha = \frac{1}{4} \ , \ \beta = \frac{1}{8} \ , \ a = \frac{1}{2} \ , \ \text{and } b = \frac{1}{4} \ .$$

There exists a corresponding expression for $\delta_y \rho_{rot(i,j)}$, and therefore the approach will render the same weights in the y-direction. They satisfy the demands of equation (2.7), and the rotated grid method can therefore indeed be interpreted as a 2nd order finite volume method.

3.3 Alternative Method E

A closer look at the equation (3.5) reveals that it simply is the 2nd order POM method from three different j-levels (in the y-direction), weighted such that they approximate the derivative of ρ in the middle cell. It is natural to attempt a similar approach with the points from Method E. The 4th order Method C is computed at three j-levels, and weighted as in the rotated grid method.
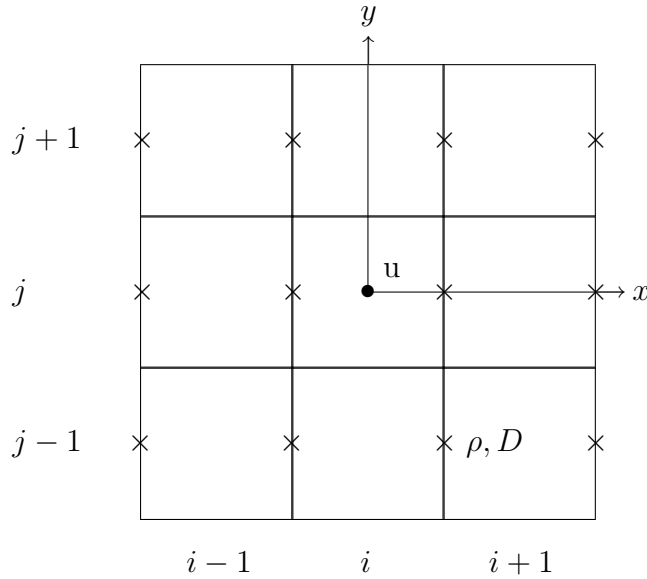
Figure 3.3: Points ρ, D ($\times$) and u ($\bullet$) at a σ-level used to construct the alternative Method E.

Recall the weights of Method C, given in (2.12). For $\frac{\partial \rho}{\partial x}|_u$, the same weights as for the rotated grid method just described are obtained. For D in a u-point, the expression becomes

$$
\begin{aligned}
D|_u \;=\; & \frac{1}{2}\left[\frac{13}{24}\left(D(i,j)+D(i-1,j)\right)-\frac{1}{24}\left(D(i+1,j)+D(i-2,j)\right)\right]+ \\
& \frac{1}{4}\left[\frac{13}{24}\left(D(i,j+1)+D(i-1,j+1)\right)-\frac{1}{24}\left(D(i+1,j+1)+D(i-2,j+1)\right)+\right. \\
& \left.\frac{13}{24}\left(D(i,j-1)+D(i-1,j-1)\right)-\frac{1}{24}\left(D(i+1,j-1)+D(i-2,j-1)\right)\right].
\end{aligned}
$$

The weights, as they would have been in equations (2.15), are

$$
\alpha=\frac{13}{48}\;,\;\; \beta=\frac{13}{96}\;,\;\; \gamma=-\frac{1}{48}\;,\;\; \delta=-\frac{1}{96}\;,
$$

$$
a=\frac{1}{2}\;,\;\; b=\frac{1}{4}\;,\;\; \text{and } c=d=0\;.
$$

These weights satisfy the equations (2.16) and (2.17), and therefore this way of utilising the points from Method E yields a 4th order method in x, like in Method C. As before, the approach will result in the same expressions for $\frac{\partial D}{\partial x}$ and ρ in a u-point, both in the x- and y-direction.

Chapter 4

Experiments

4.1 The seamount case

As mentioned earlier, using test cases featuring the steep topography of a tall, narrow seamount is an effective way of revealing internal pressure gradient errors. The case was first studied by Beckmann and Haidvogel in 1993. Now it is a common test case, treated in e.g. [Mellor et al., 1998], [Shchepetkin and McWilliams, 2003], and [Berntsen and Oey, 2010].

The setup of the model will be identical to that of the experiments in [Berntsen and Oey, 2010], so as to make it possible to compare the results. The topography in this study is given as

$$H(x, y) = H_0 \left(1.0 - 0.90 e^{-(x^2 + y^2)/L^2} \right). \tag{4.1}$$

Here, H_0 is $4500\,\text{m}$ and L is $40\,\text{km}$, see Figure 4.1.

The seamount is placed in the centre of a channel of length $390\,\text{km}$ and width $294\,\text{km}$. The boundaries are closed at $x = 0\,\text{km}$, $x = 390\,\text{km}$, $y = 0\,\text{km}$ and $y = 294\,\text{km}$.

The initial reference stratification is defined to be

$$\rho_{ref}(z) = 28\,\text{kgm}^{-3} - \Delta\rho e^{\frac{z}{500\text{m}}} \tag{4.2}$$

where $\Delta\rho = 3.263\,\text{kgm}^{-3}$. The initial perturbation density is defined as

$$\rho'(z) = 1.5\,\text{kgm}^{-3} e^{\frac{z}{500\text{m}}}. \tag{4.3}$$

The Burger number
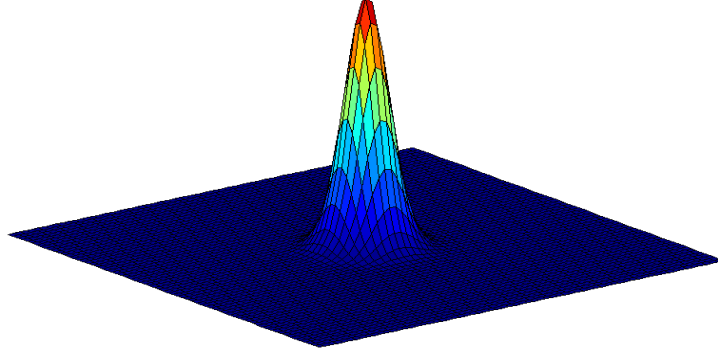
Figure 4.1: The seamount

$$S = \frac{\sqrt{gH_0\Delta\rho/\rho_0}}{fL} \ , \tag{4.4}$$

is a measure of stratification in presence of rotation [Cushman-Roisin, 1994]. It is 3.0 for the present set of parameters.

Furthermore, $\Delta x = \Delta y = 6\,\mathrm{km}$ and the Coriolis parameter is constant and equal to $10^{-4}\,\mathrm{s}^{-1}$. The horizontal viscosity A_M is $100\,\mathrm{m}^2\mathrm{s}^{-1}$. The model is run with 40 equidistant layers.

There is no external forcing, and the stratification is stable, so all velocities should always equal zero. However, the internal pressure gradient error will set the system in motion. Therefore the maximum velocity and kinetic energy will be an estimate of the error.

The kinetic energy is computed according to

$$E_{kin} = \frac{1}{2V}\sum_{i,j,k}\left[\triangle V_{i+\frac{1}{2},j,k}u^2_{i+\frac{1}{2},j,k} + \triangle V_{i,j+\frac{1}{2},k}v^2_{i,j+\frac{1}{2},k}\right] \ ,$$

and the maximum velocity is

$$V_{max} = \max\left[\sqrt{u^2_{i,j,k} + v^2_{i,j,k}}\right] \ .$$

Also,

$$V = \sum_{i,j,k} \triangle V_{i,j,k}$$

is the total volume of the domain. $\triangle V_{i,j,k}$, $\triangle V_{i+\frac{1}{2},j,k}$, and $\triangle V_{i,j+\frac{1}{2},k}$ are control volumes of ρ, u, and v-point grid boxes respectively.

4.2   The Method B_α experiments

The seamount test case can be used to investigate whether a weighted combination of methods (as discussed in Chapter 3 and [Thiem and Berntsen, 2006]) can give improved results. If there indeed exists a cancellation of errors, the optimal *fixed* weighting of the standard 2nd order POM and the rotated grid method from Section 3.2 will be sought.

To outline how the new internal pressure gradient actually will be computed in a point (x, y, σ), at a time t, consider its x-component,

$$\text{IPG}_x(x, y, \sigma, t) = \alpha \cdot \text{IPG}_x^2(x, y, \sigma, t) + (1 - \alpha) \cdot \text{IPG}_x^{2,4}(x, y, \sigma, t) \, , \quad (4.5)$$

where $\text{IPG}_x^2(x, y, \sigma, t)$ is the internal pressure gradient computed with the 2nd order POM method, and $\text{IPG}_x^{2,4}(x, y, \sigma, t)$ is the pressure gradient given by the rotated grid method from Section 3.2. The superscripts indicate the number and position of the applied points. The first number represents the points included on the jth level, the next number shows how many points are included symmetrically above and below, at level $(j - 1)$ and $(j + 1)$ combined. See Figures 2.4 and 2.5.

The value $\alpha = 0$ in (4.5) corresponds to the 2nd order POM method, and $\alpha = 1$ gives the pure rotated grid method. The same expression is valid for the y-direction (but with the stencils from Figures 2.4 and 2.5 rotated 90 degrees).

The new rotated grid and the 2nd order POM pressure gradients are computed in every cell, before they are weighted against each other. The kinetic energy and the maximum velocity are taken out after 10 days for different values of α. The value of α is set to some fixed number between 0 and 1 for each run, with intervals of length 0.05, see Figure 4.2.

For values of α below 0.4, the error is even larger than for the values plotted. When the rotated grid method is dominant, (for values of α close to zero) the model run is terminated before 10 days because of instability. These results are not included, since the region of interest clearly lies in the other end of the interval.

Since the energy should be as small as possible, the minimum point of this graph is the point of greatest interest. It appears to be somewhere between $\alpha = 0.85$ and $\alpha = 0.9$. The weight is therefore fixed at $\alpha = 0.875$, and from this point, the resulting method will be called Method B_α. Experimenting with different weighting confirms that this estimate for a fixed value of α seems to be the optimal choice, even when the model is run for 180 days.

The fact that there appears to be a cancellation of errors with this value of α is consistent with what was found in [Thiem and Berntsen, 2006]. The
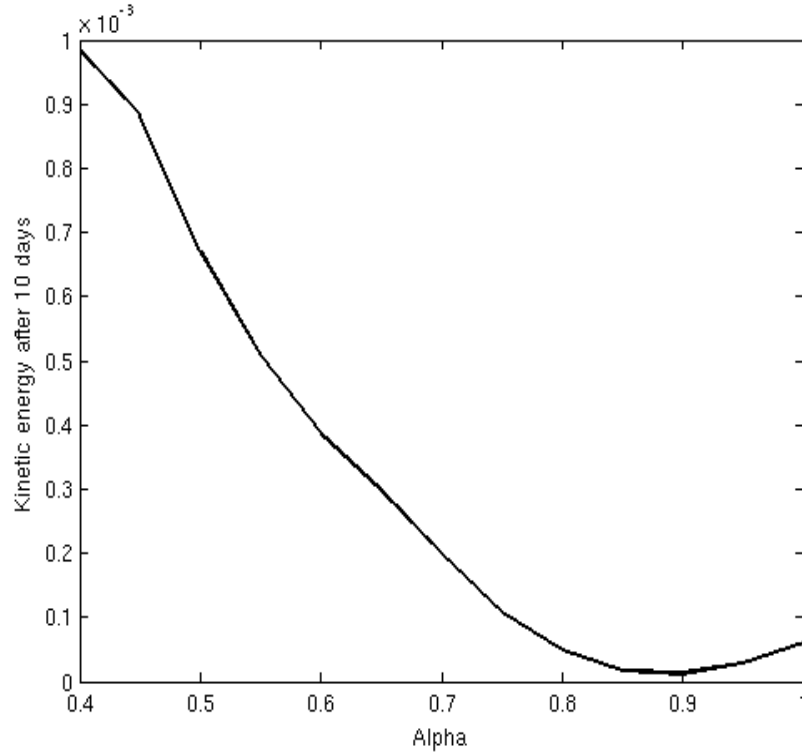
Figure 4.2: The kinetic energy after 10 days as a function of α for the Method B_α experiments.

$4-1$ weighting for which the error was reduced, corresponds to $\alpha = 0.8$.

4.3 The Method E_α experiments

By using the same weights as for the rotated grid method (as discussed in Section 3.3), a new method based on Method C can be constructed. The internal pressure gradient in the x-direction is computed according to

$$\text{IPG}_x(x, y, \sigma, t) = \alpha \cdot \text{IPG}_x^4(x, y, \sigma, t) + (1 - \alpha) \cdot \text{IPG}_x^{4,8}(x, y, \sigma, t) \ .$$

The superscripts indicate the number and position of the applied points, as above. Recall the stencils in Figures 2.6 and 2.8. The same expression applies for the y-direction.

An estimate of the optimal fixed value of α can be found with a similar experiment. Below, the kinetic energy after 10 days is plotted for values of
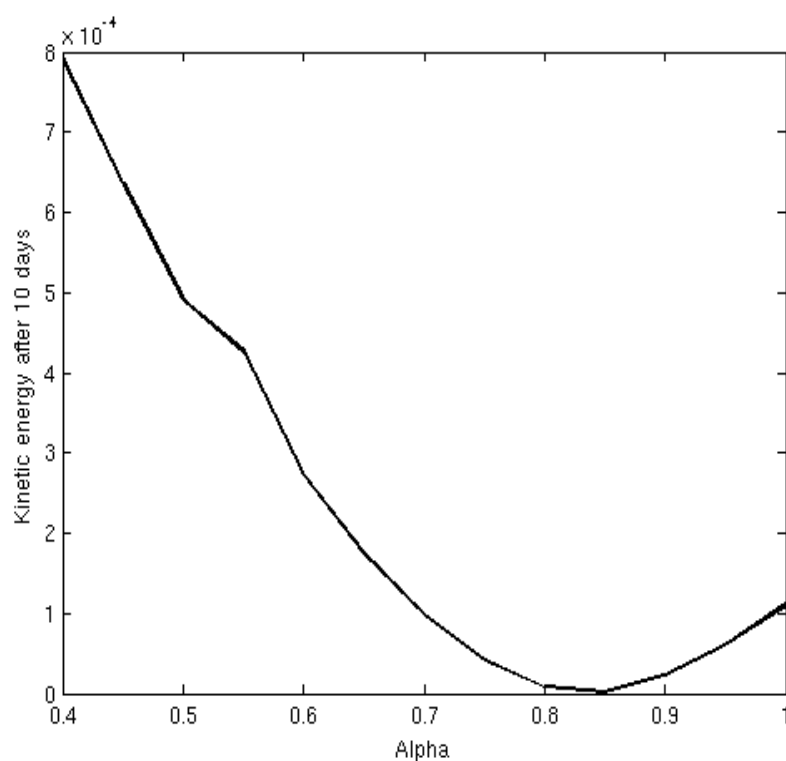
Figure 4.3: The kinetic energy after 10 days as a function of α for the Method
E_α experiments.

α between 0.4 and 1, see Figure 4.3. To make the minimum point easier to
find graphically, the values of α below 0.4 are excluded. The error grows as
α approaches zero. The methods seem to interact in much the same way as
the 2nd order POM and the rotated grid method.

In the plot of the energy (Figure 4.3), the error seems to reach its mini-
mum somewhere between $\alpha = 0.80$ and $\alpha = 0.85$. The weight α is fixed at
the value 0.825, and the result is called Method E_α.

Chapter 5

Initial vorticity and SESK

The description of the Sigma Errors of the Second Kind (SESK) from [Mellor et al., 1998] clearly motivates a study of the vorticity-related errors of the methods previously developed. According to Mellor et al. [1998], the SESK appearing in 3D experiments are the errors of greatest concern, since they tend to not die out prognostically.

By using the initial pressure forces to calculate the initial acceleration of the vorticity, a measure of the internal pressure gradient errors and possible improvements can be obtained. It leads to an economical way of anticipating how well the methods will perform.

5.1   Results for the methods

The vertically integrated initial acceleration of the vorticity,

$$\frac{\partial}{\partial t} \int_{-1}^{0} \left[\frac{\partial v}{\partial x} - \frac{\partial u}{\partial y} \right] d\sigma \;,$$

is computed.

The 2nd order POM method (Method A) gives the results seen in Figure 5.1(a). This eight-lobed pattern is a typical display of the SESK that appear around the steep topography of the seamount. The plot presents a visual motivation for the rotated grid method from Chapter 3. The flow in each of the neighbouring vortices are oppositely directed, and one can imagine that a 45 degree rotation should cancel the errors.

In Figure 5.1, plots of the initial acceleration of the vorticity for each of the methods previously developed are included.

From this, one should in particular expect the fourth order Method D and Method E_α to deliver good results.

(a) Method A

(b) Method B$_\alpha$

(c) Method C
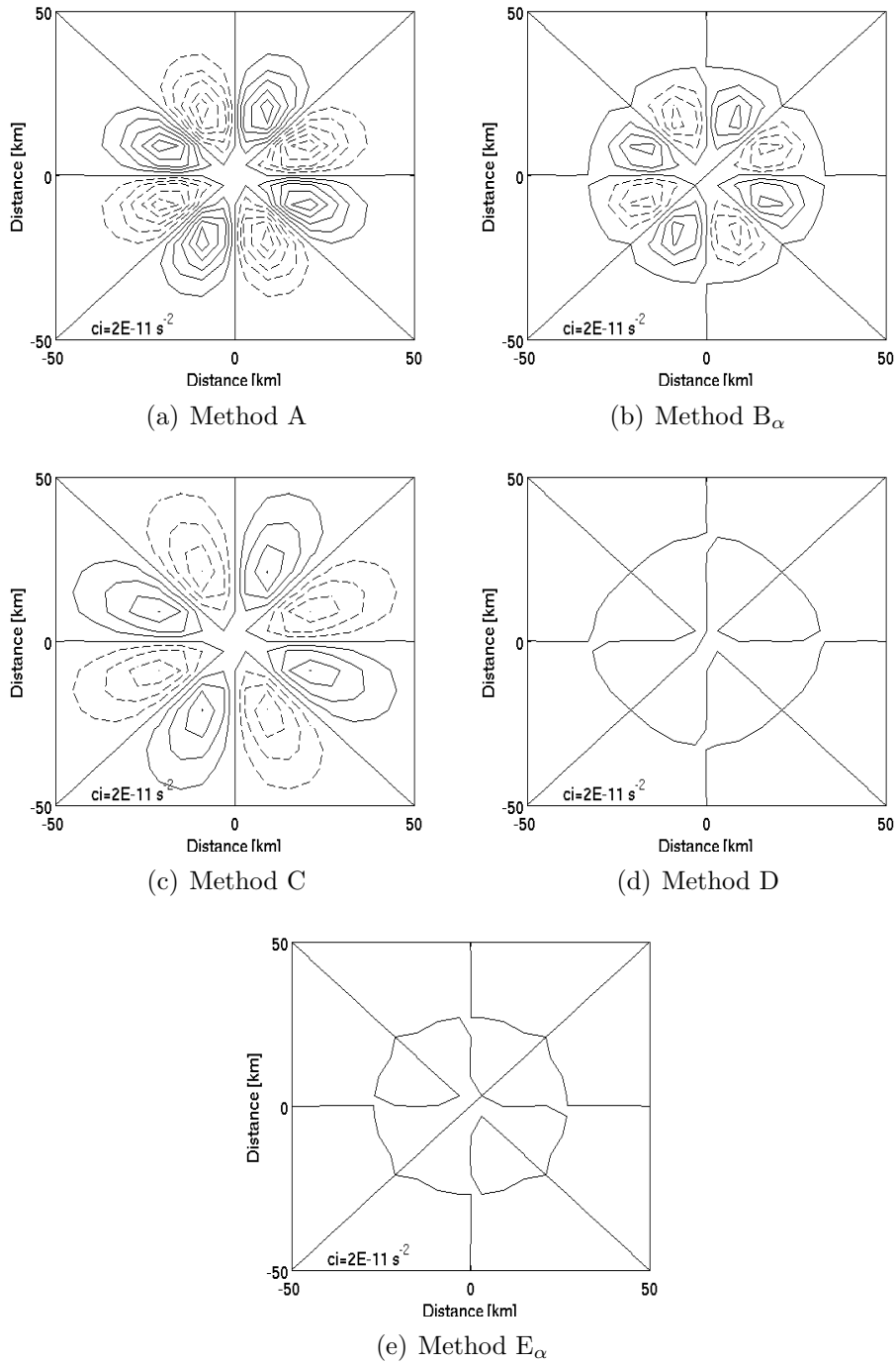
(d) Method D

(e) Method E$_\alpha$

Figure 5.1: The vertically integrated initial acceleration of the vorticity for each of the discussed methods.

5.2 The weighted methods: Elimination of the initial vorticity

The following plot series gives an impression of why the weighted Method B$_\alpha$ displays a reduced error, and why the best fixed values are such that the original method is dominant. The vortices of the rotated approach are larger and oppositely directed. A smaller version of these vortices added to the original vortices should intuitively lead to a cancellation. This is in fact what seems to happen, see Figure 5.2. However, the cancellation is not complete.

The alternative Method E and Method C interact in the same way, although they seem to be a slightly better fit, see Figure 5.3. Note that the shapes of the vortices for the two separate methods appear to be quite similar.

(a) $\alpha = 0$.

(b) $\alpha = 0.5$

(c) $\alpha = 0.7$

(d) $\alpha = 0.8$

(e) $\alpha = 0.9$

(f) $\alpha = 1$.
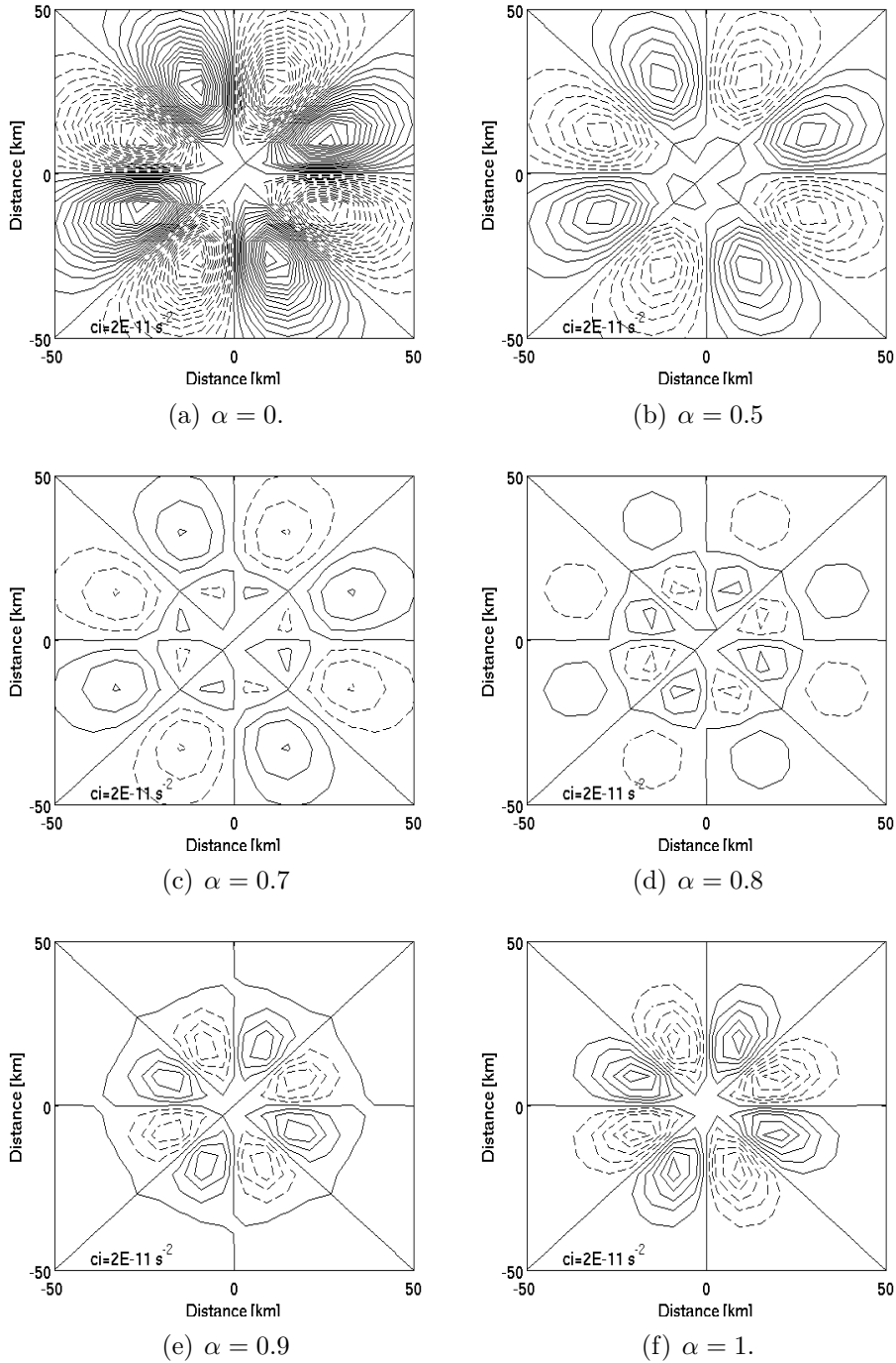
Figure 5.2: The vertically integrated initial acceleration of the vorticity for the combination of the rotated grid approach and standard 2nd order POM, different fixed weights.

(a) $\alpha = 0$.

(b) $\alpha = 0.5$

(c) $\alpha = 0.7$

(d) $\alpha = 0.8$

(e) $\alpha = 0.9$

(f) $\alpha = 1$.
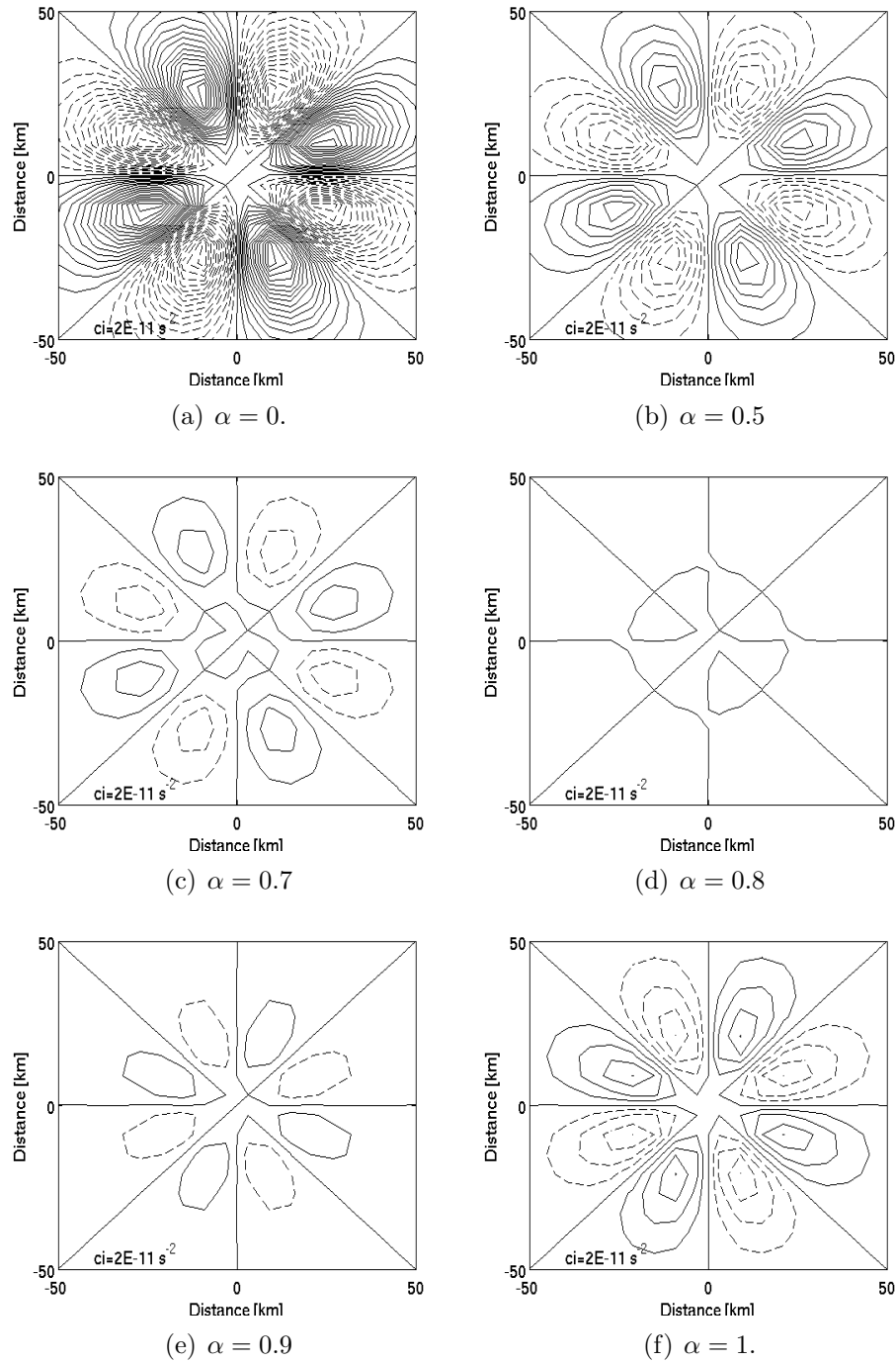
Figure 5.3: The vertically integrated initial acceleration of the vorticity for the combination of the alternative Method E and the Method C, different fixed weights.

Chapter 6

The optimal weighting

The experiments with the weighted approaches suggest that there is an interaction between the methods that leads to a cancellation of errors. It is tempting to investigate this further, and try a new, more complex manner of weighting.

Now, assume that two estimates of the erroneous internal pressure forces in a u-point has been found, corresponding to each of the two methods involved. If the estimates are of opposite signs and comparable in magnitude, a weight between 0 and 1 can be found such that a combination of the two will equal zero. The method can then be defined by a three-dimensional field of weights, instead of by a single fixed constant. Ideally, it would only be necessary to compute the weights once, before the model is propagated in time. The error, and consequently the weights, will only depend on the topography, the stratification and the grid size.

It is necessary to demand that the value of the weight is between 0 and 1, to ensure a stable result. Weights outside of this interval will imply that an extrapolation of the internal pressure functions is needed, and that is generally a more unstable process than interpolation. Of course, this means that it is crucial for the two methods to be a 'perfect fit' for the approach to be successful.

This idea is in many ways similar to the approach proposed by Stelling and Van Kester [1994]. They estimated the internal pressure in z-coordinates in two different ways. The approach ensured that the estimates frequently became of opposite sign. The gradient were in these cases set to zero. When the estimates were of the same sign, the smaller value was utilised. Even though the approach gave promising results, the calculations involved were rather complex. In addition, Slørdal [1997] showed that the approach generally underestimated the geostrophic flow. The approach of optimal weighting in principle is a simple and straightforward computation.

Two separate fields of weights will be needed; one for the x-direction and one for the y-direction. The focus will still be on the x-component, and the weights will be called $\alpha_x(x, y, \sigma)$.

6.1 Finding $\alpha_x(x, y, \sigma)$

When the discretisations are based on the following integral

$$\frac{\partial p}{\partial x} = g \int_\sigma^0 \left(D\frac{\partial \rho}{\partial x} + \frac{\partial D}{\partial x}\rho \right) d\sigma + g\sigma\rho\frac{\partial D}{\partial x} \; , \tag{6.1}$$

as they have been up to this point, the vertical integration has to be computed before the weighting is done. In other words, the errors in each layer are added up. If the error is eliminated before the integration is done, better results can be expected.

In this chapter, discretisations based on the other form of the integral from Chapter 1 will be considered,

$$\frac{\partial p}{\partial x} = gD \int_\sigma^0 \left(\frac{\partial \rho}{\partial x} - \frac{\sigma}{D}\frac{\partial \rho}{\partial \sigma}\frac{\partial D}{\partial x} \right) d\sigma \; . \tag{6.2}$$

Initially, two estimates of the integrand will be made. The weights will be constructed so that the integrand is zero when the value of the weight in some u-point is between 0 and 1. If the expression for the internal pressure gradient from (6.2) is used, it will suffice to consider a weighted approach of the integrand, since the integral should be zero when the integrand is.

The estimate of the integrand in (6.2) computed with the standard 2nd order POM method is called $\mathrm{FINT}_x^2(x, y, \sigma, t)$, and the same estimate computed with the rotated grid method from Chapter 3 is called $\mathrm{FINT}_x^{2,4}(x, y, \sigma, t)$. The superscripts indicate the number and position of the applied points, as in Section 4.2.

For a given cell (x, y, σ), at the time $t = 0$, it is required that

$$\alpha_x(x, y, \sigma) \cdot \mathrm{FINT}_x^2(x, y, \sigma, 0) + [1 - \alpha_x(x, y, \sigma)] \cdot \mathrm{FINT}_x^{2,4}(x, y, \sigma, 0) \;\; = \;\; 0 \; .$$

This gives the following expression for the weight

$$\alpha_x(x, y, \sigma) \;\; = \;\; \frac{\mathrm{FINT}_x^{2,4}(x, y, \sigma, 0)}{\mathrm{FINT}_x^{2,4}(x, y, \sigma, 0) - \mathrm{FINT}_x^2(x, y, \sigma, 0)} \; .$$

If the value of $\alpha_x(x, y, \sigma)$ is in the desired range, it will be used. If this is not the case, the smaller of the two estimates will be used. Ideally, once the weights are computed, they can be applied for the whole experiment, and other experiments with the same topography, grid size, and similar stratification.

The results of this approach is dependent on the weights actually being between 0 and 1. The seamount test case will be applied, and $\alpha_x(x, y, \sigma)$ will be investigated.

6.2   Investigations around the seamount

The following plots are vertical profiles of the value of both the original initial integrand values, $\text{FINT}_x^2(x, y, \sigma, 0)$ and $\text{FINT}_x^{2,4}(x, y, \sigma, 0)$, and the initial value of the final integrand, $\text{FINT}_x(x, y, \sigma, 0)$ in a small area around the seamount (Figure 6.1). The middle cell in Figure 6.1 is the middle cell of the whole test basin. The eight neighbouring cells are included.

The purpose of the investigation is to find out whether the two methods are suited for this approach. The corresponding vertical profiles of $\alpha_x(x, y, \sigma)$ are also included.
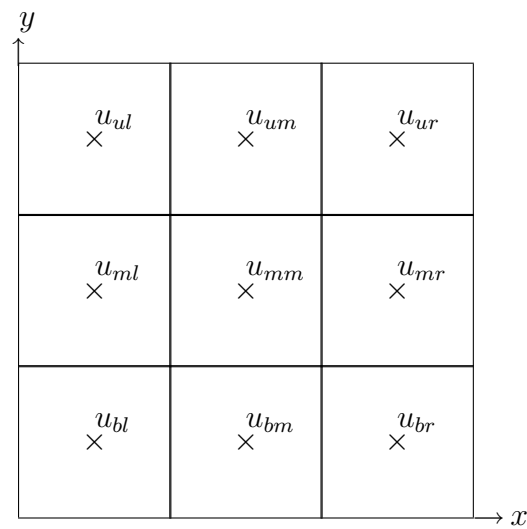
Figure 6.1: The area around the seamount, in which we investigate the effects of the optimal weighting. ($\times$) marks the u-points. Subscript gives the position. 'u' stands for 'upper', 'm' stands for middle, 'b' stands for 'bottom'. 'l' stands for 'left', 'm' stands for 'middle', 'r' stands for 'right'.

(a) Plot for u_{ul}

(b) Plot for u_{ul}

(c) Plot for u_{ml}

(d) Plot for u_{ml}

(e) Plot for u_{bl}

(f) Plot for u_{bl}
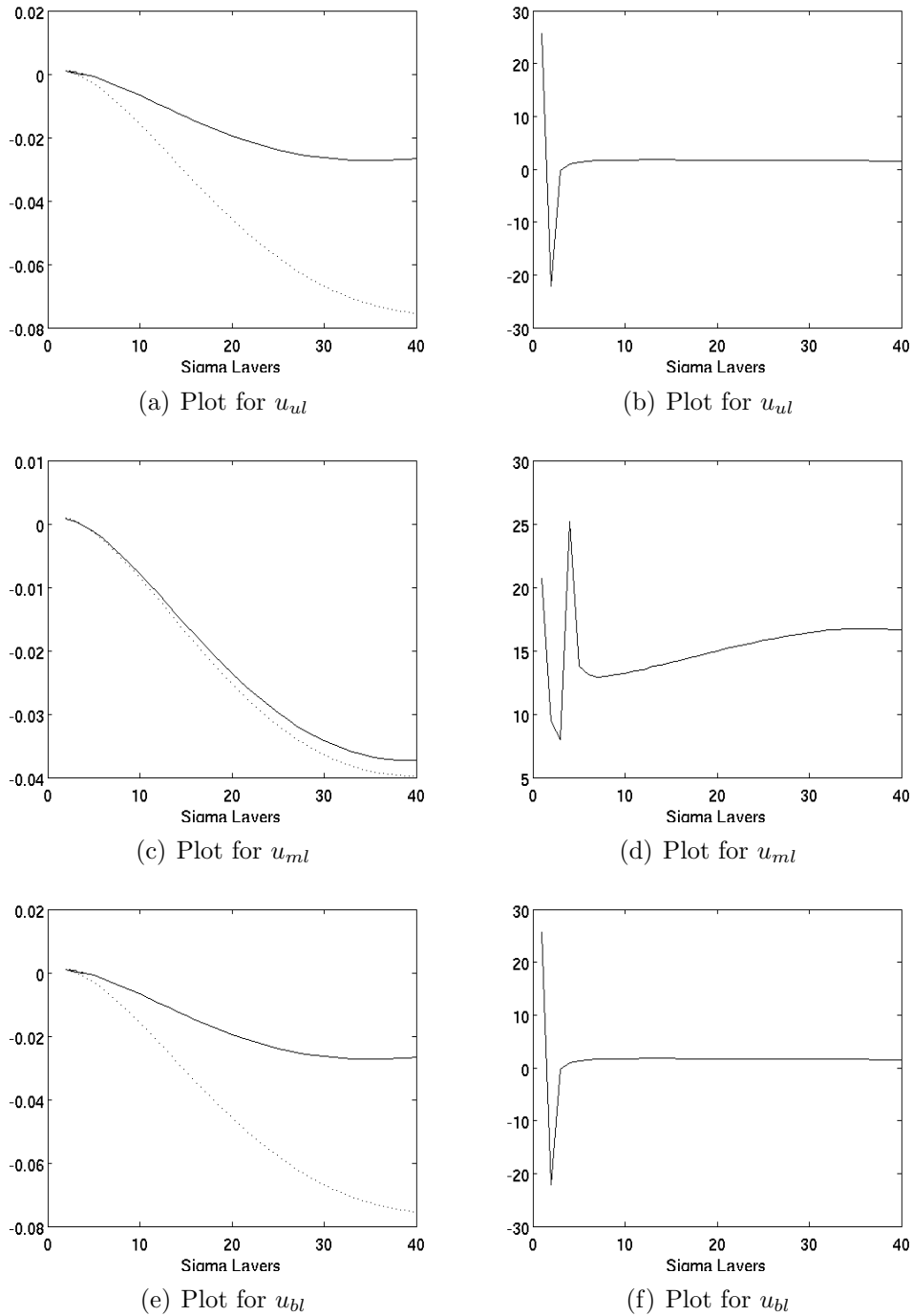
Figure 6.2: Plots for the three cells on the left side. To the left, the dashed line represents $\mathrm{FINT}_x^2(x, y, \sigma, 0)$, the dotted line represents $\mathrm{FINT}_x^{2,4}(x, y, \sigma, 0)$, and the solid line represents the best approximation. Note that the solid line covers the dashed line almost completely. The plots to the right show the vertical profile of $\alpha_x(x, y, \sigma)$ in the given point.

(a) Plot for u_{um}

(b) Plot for u_{um}

(c) Plot for u_{mm}

(d) Plot for u_{mm}

(e) Plot for u_{bm}

(f) Plot for u_{bm}
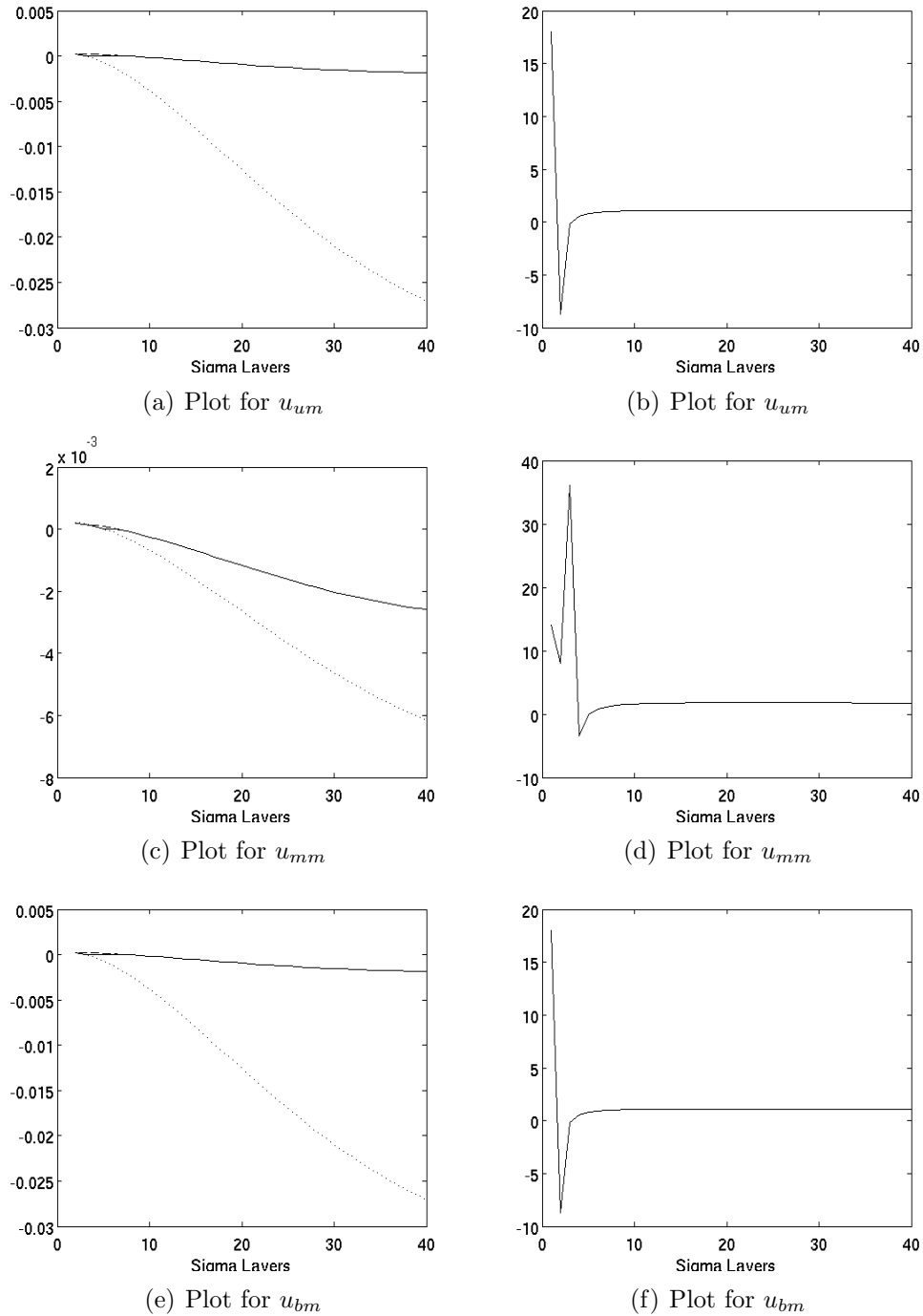
Figure 6.3: Plots for the three cells in the middle. To the left, the dashed line represents $\mathrm{FINT}_x^2(x, y, \sigma, 0)$, the dotted line represents $\mathrm{FINT}_x^{2,4}(x, y, \sigma, 0)$, and the solid line represents the best approximation. Note that the solid line covers the dashed line almost completely. The plots to the right show the vertical profile of $\alpha_x(x, y, \sigma)$ in the given point.

(a) Plot for u_{ur}

(b) Plot for u_{ur}

(c) Plot for u_{mr}

(d) Plot for u_{mr}

(e) Plot for u_{br}

(f) Plot for u_{br}
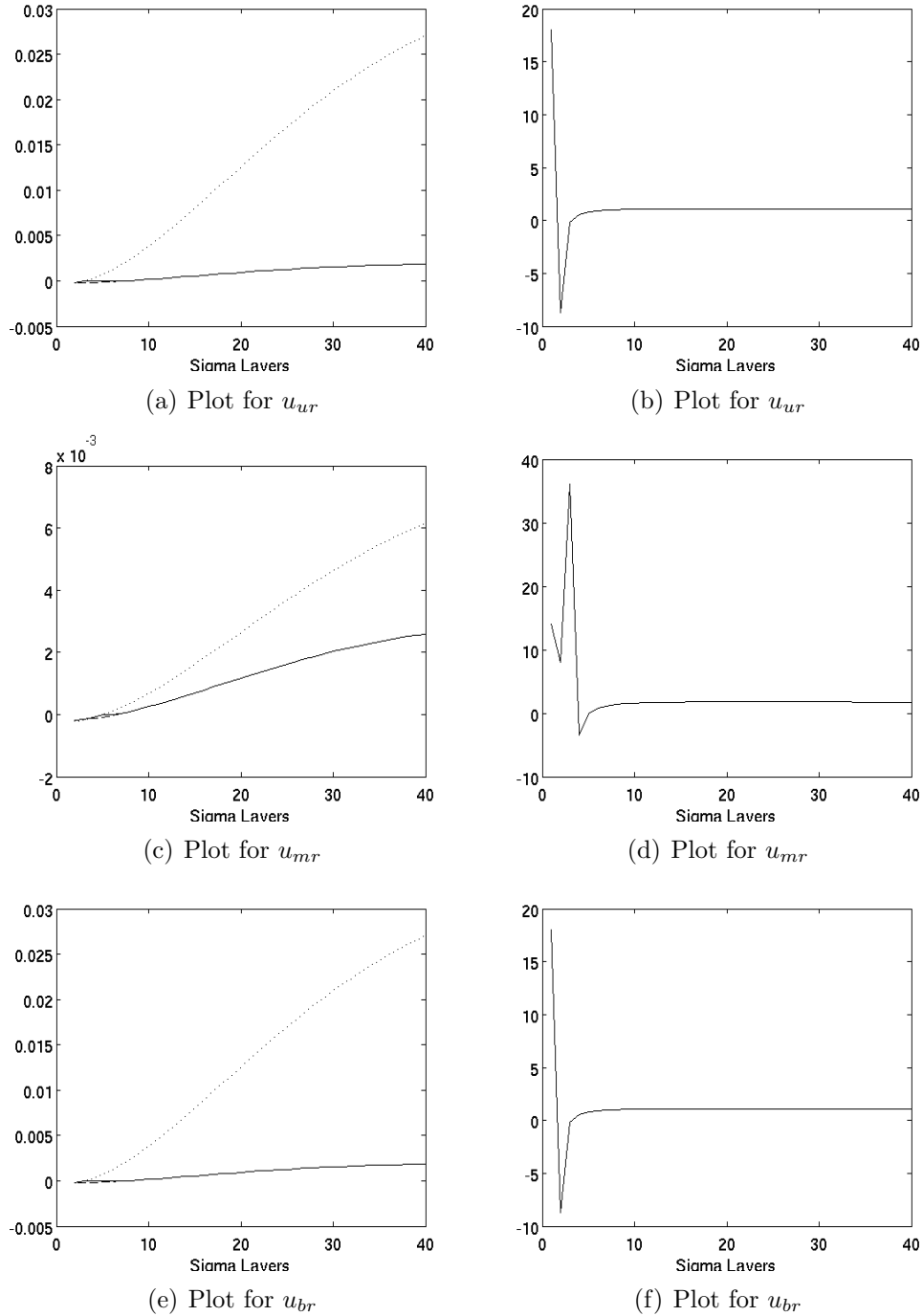
Figure 6.4: Plots for the three cells on the right side. To the left, the dashed line represents $\mathrm{FINT}_x^2(x, y, \sigma, 0)$, the dotted line represents $\mathrm{FINT}_x^{2,4}(x, y, \sigma, 0)$, and the solid line represents the best approximation. Note that the solid line covers the dashed line almost completely. The plots to the right show the vertical profile of $\alpha_x(x, y, \sigma)$ in the given point.

At the points where the weighting actually has been done, the integrand value is reduced to zero. Note the symmetry around the three middle cells.

Unfortunately, the two internal pressure gradient estimates do not satisfy the necessary criteria for a complete cancellation. Typically, the eliminations only occur in a few of the upper layers, see Figure 6.5.
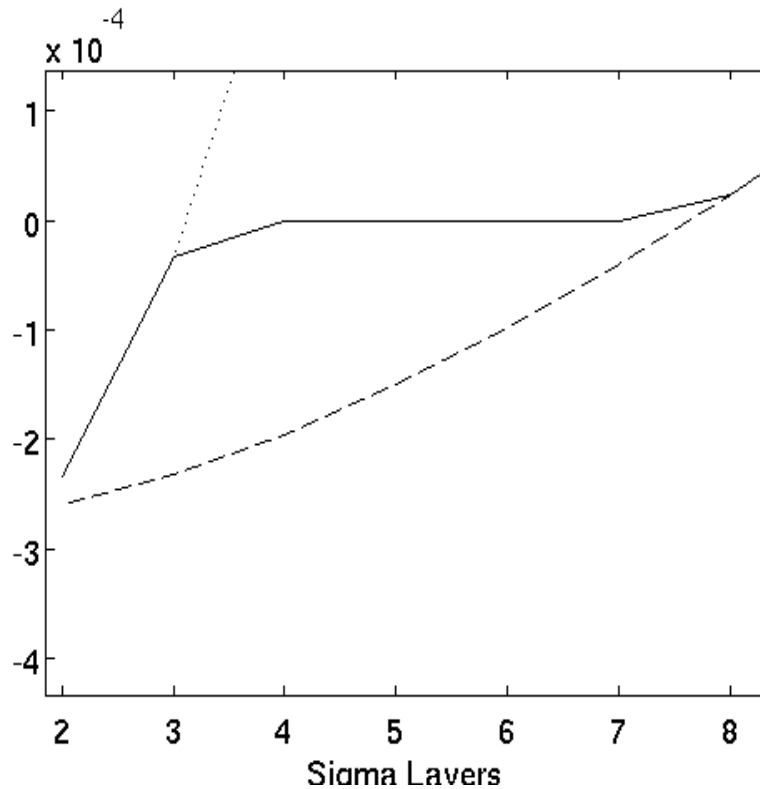
Figure 6.5: A zoom-in on the area where the error elimination has been done. The dashed line represents $\text{FINT}_x^2(x, y, \sigma, 0)$, the dotted line represents $\text{FINT}_x^{2,4}(x, y, \sigma, 0)$, and the solid line represents the best approximation.

The sudden drop to zero of the internal pressure gradient can potentially create a sharp discontinuity, and lead to severe instabilities. This probably would be a problem regardless of if more of the weights were in the desired range, that is, as long as the optimal weighting does not deliver perfect results.

Plots of $\alpha_x(x, y, \sigma)$ for different values of σ in an area around the seamount are also included, see Figure 6.6.
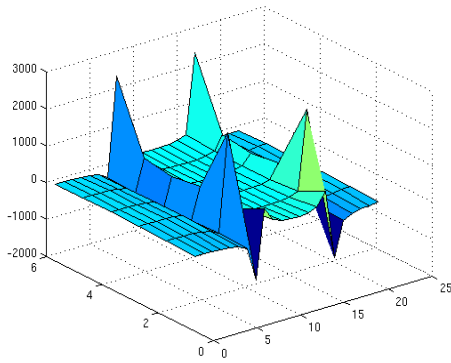
(a) Plot for $\sigma = 1$
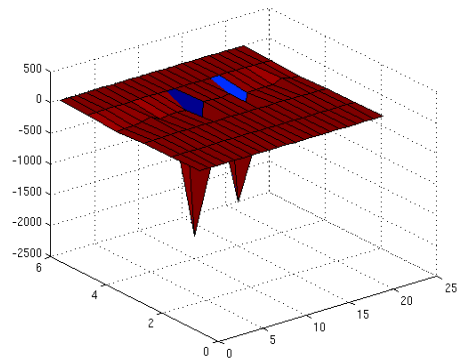
(b) Plot for $\sigma = 10$
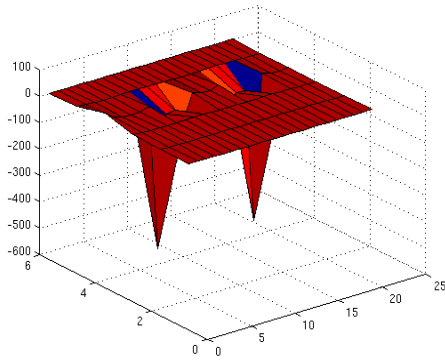
(c) Plot for $\sigma = 20$
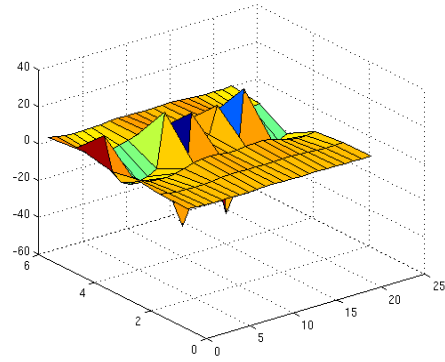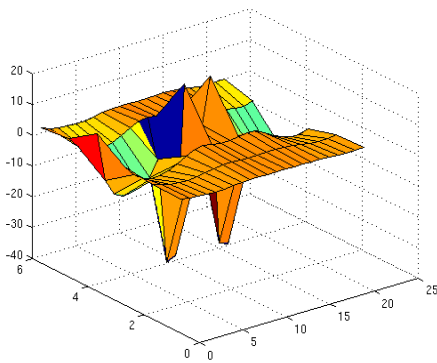
(d) Plot for $\sigma = 30$

(e) Plot for $\sigma = 35$
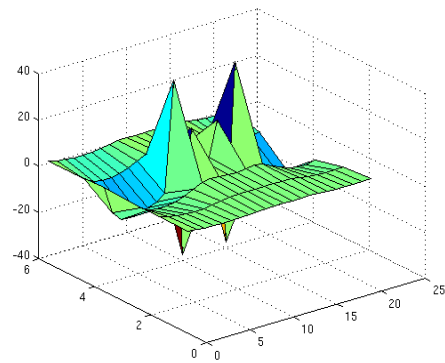
(f) Plot for $\sigma = 40$

Figure 6.6: Plot of $\alpha_x(x, y, \sigma)$ for different σ-layers

6.2.1 Shapiro filtering

The field of weights exhibits several singularities, and does not appear to be particularly smooth. To remedy this, it is possible to use a linear filtering technique. Consequently, a *Shapiro filter* [Shapiro, 1975] was applied in all spatial directions, for the entire model domain. Consider the filtering in the x-direction, given by

$$\overline{\alpha}_x(i,j,k) = \frac{1}{4}\alpha_x(i-1,j,k) + \frac{1}{2}\alpha_x(i,j,k) + \frac{1}{4}\alpha_x(i+1,j,k) , \qquad (6.3)$$

where i, j and k are the discrete coordinates in the x-, y-, and σ-direction, respectively.

Shapiro filtering only once gave no visible impact on the integrand values around the seamount – the results were similar to the Figures 6.2, 6.3 and 6.4, even though the vertical profile of $\alpha_x(x,y,\sigma)$ in the given point clearly became smoother. See Figure 6.7 for the point u_{ur}.
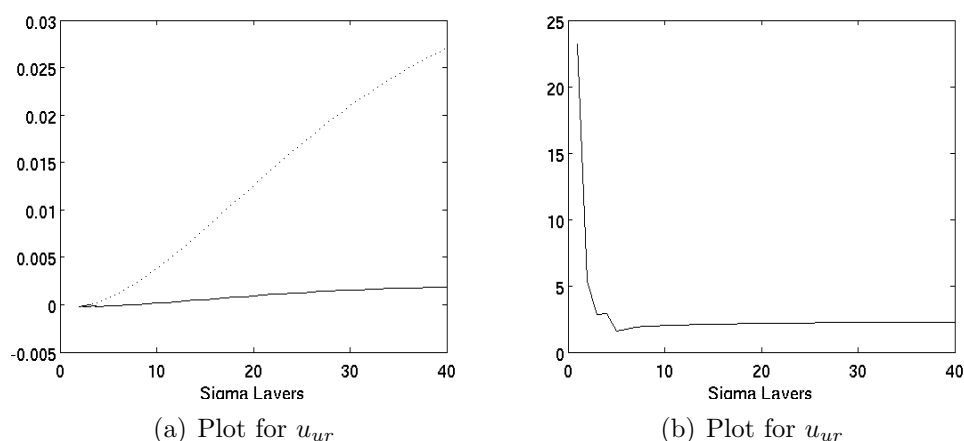

| (a) Plot for u_{ur} | (b) Plot for u_{ur} |

Figure 6.7: Shapiro-filtered once. To the left, the dashed line represents $\text{FINT}_x^2(x,y,\sigma,0)$, the dotted line represents $\text{FINT}_x^{2,4}(x,y,\sigma,0)$, and the solid line represents the best approximation. The plot to the right shows the vertical profile of $\alpha_x(x,y,\sigma)$ in the given point.

To investigate the effects of further smoothing, the Shapiro filter was applied three times to $\alpha_x(x,y,\sigma)$, see Figure 6.8.

The experiments reveal a possible danger to Shapiro filtering $\alpha_x(x,y,\sigma)$. It becomes evident when filtering a field where so many of the weights are not in the interval between 0 and 1. Some false weights, which are originally not in the desired range, can suddenly appear. They create new, even sharper discontinuities, see Figure 6.9 for an illustration.
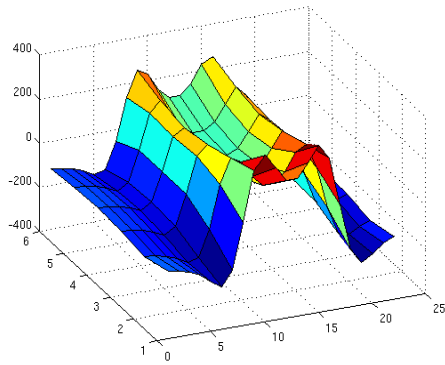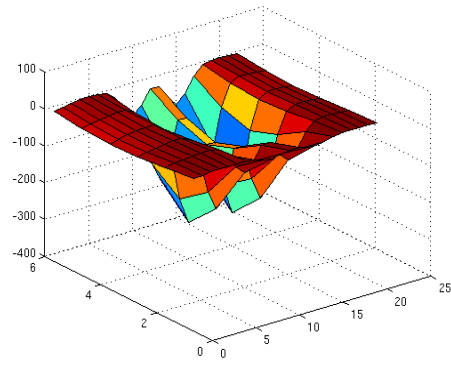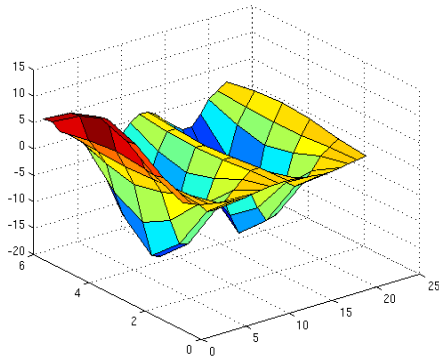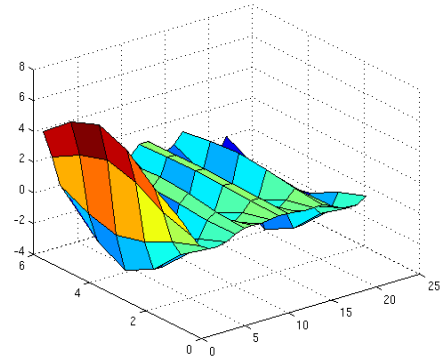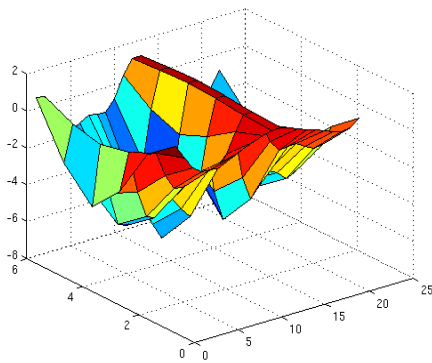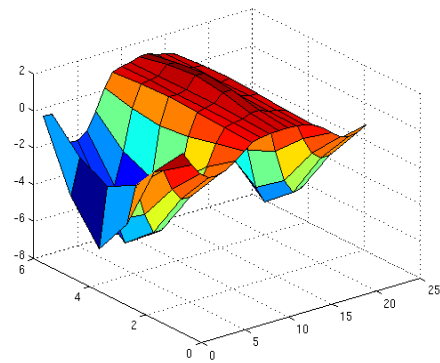
(a) Plot for $\sigma = 1$

(b) Plot for $\sigma = 10$

(c) Plot for $\sigma = 20$

(d) Plot for $\sigma = 30$

(e) Plot for $\sigma = 35$

(f) Plot for $\sigma = 40$

Figure 6.8: Plot of $\alpha_x(x, y, \sigma)$ for different σ-layers, Shapiro filter applied three times.

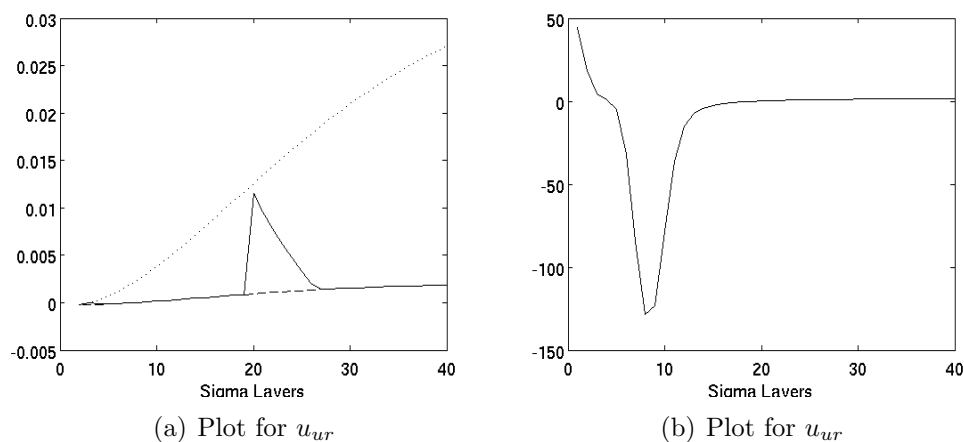(a) Plot for u_{ur} (b) Plot for u_{ur}

Figure 6.9: The weights $\alpha_x(x, y, \sigma)$, Shapiro-filtered three times. To the left, the dashed line represents $\mathrm{FINT}_x^2(x, y, \sigma, 0)$, the dotted line represents $\mathrm{FINT}_x^{2,4}(x, y, \sigma, 0)$, and the solid line represents the best approximation. The plot to the right shows the vertical profile of $\alpha_x(x, y, \sigma)$ in the given point.

6.2.2 The reappearance of the fixed weight

It was experimented with setting the weights to 0.875 (which is the fixed weight obtained in Section 4.2), when they were not between 0 and 1. This differs from the approach from above, where the smaller of the two estimates were used.

Even though this approach also results in some discontinuities (see Figure 6.10), no instabilities were encountered. The field is still much smoother, and the optimal weights are so seldom in the desired interval that the fixed weighting is most significant for the results. However, the results are slightly worse than for the Method B_α, so there is no beneficial effect of the optimal weighting in this case.

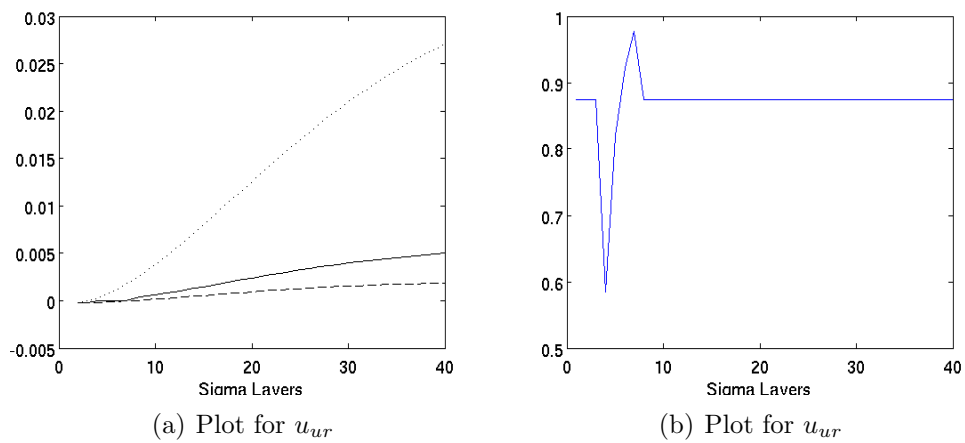(a) Plot for u_{ur} (b) Plot for u_{ur}

Figure 6.10: No filtering, but with fixed weight instead of the smaller estimate. To the left, the dashed line represents $\text{FINT}_x^2(x, y, \sigma, 0)$, the dotted line represents $\text{FINT}_x^{2,4}(x, y, \sigma, 0)$, and the solid line represents the approximation. The plot to the right shows the vertical profile of $\alpha_x(x, y, \sigma)$ in the given point.

Chapter 7

Results

The methods from the previous chapters are all applied to the seamount case, and the model is run for 180 days. The kinetic energy and the maximum velocity are taken out after each day.

This test has been performed for new numerical methods in several previous studies, see for example [Shchepetkin and McWilliams, 2003] and [Berntsen and Oey, 2010]. It gives a good impression of the long term stability of the approaches.

7.1 Comments on the finite volume methods

The kinetic energy for each method is plotted in Figure 7.1. The optimal weighting approach from Chapter 6 is not included, as it causes the model run to go unstable within 5 days (see Section 7.2). Remember that the Method A is equal to the standard 2nd order POM method, so the performance of this method will provide a reference to which the others can be compared.

Even though Method C gives the largest values here, the graph seems to flatten more than the graph for Method A. This may indicate that the robustness is increased by applying the two extra points, recall Figure 2.6.

The Methods B_α and E_α are supposed to be improved versions of the Methods A and C, respectively. Indeed, this seems to be the case. The better performance of Method B_α is consistent with the results from [Thiem and Berntsen, 2006]. The difference between Method C and Method E_α is even larger, and quite remarkable. There certainly seems to be some error cancellation at work.

The Method D clearly gives the best results here. Recall that this is a fourth order method in both x and y.

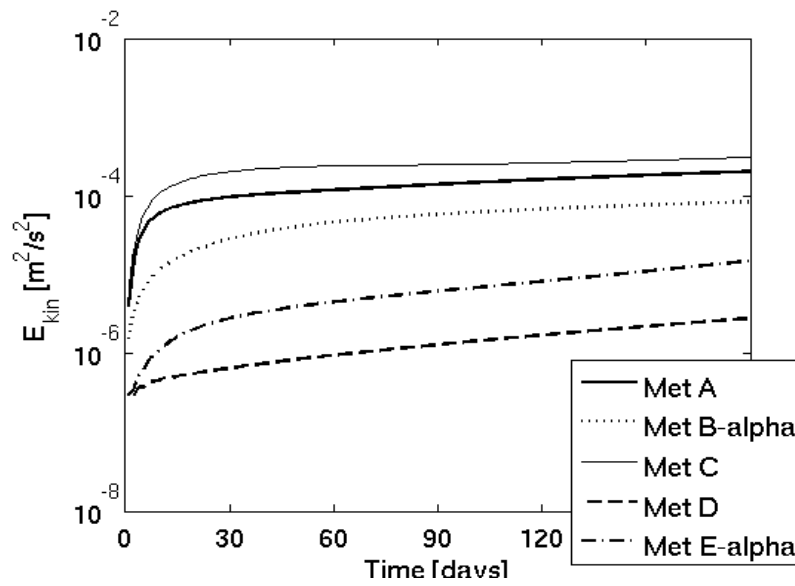A plot of the maximum velocities for the 180 days runs is also included.

Figure 7.1: Kinetic energy for the methods

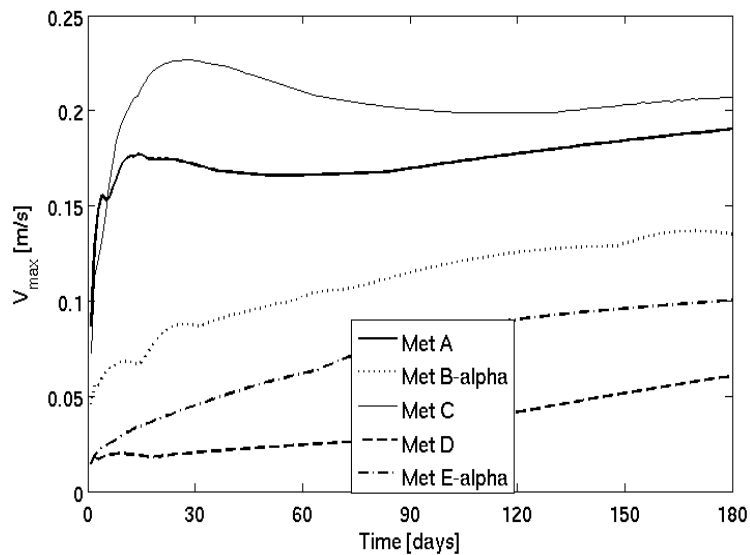These results are consistent with the kinetic energy values, see Figure 7.2.

Figure 7.2: Maximum velocity for the methods

7.2   Results for the optimal weighting approach

The experiments with the optimal weighting resulted in severe instabilities that caused the model run to be terminated before 10 days. See Figure 7.3 for the maximum velocity of the approach with unsmoothed weight fields ($\alpha_x(x, y, \sigma)$ and $\alpha_y(x, y, \sigma)$ without Shapiro filtering), plotted together with the finite volume methods from above.

In Figure 7.4, the maximum velocities for the optimal weights, Shapiro filtered once and thrice, are compared to the results for the optimal weighting with no filtering. The filtering has no beneficial effect in this case.
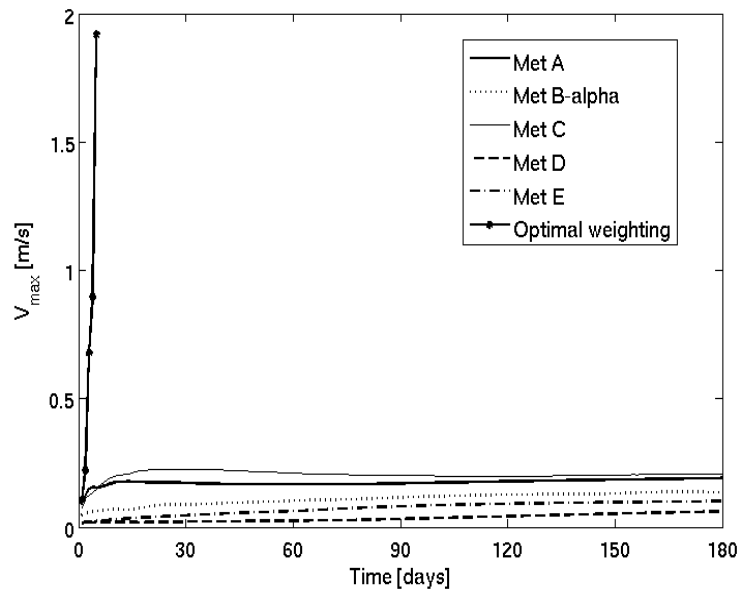

Figure 7.3: Maximum velocity for the methods, including the optimal weighting approach.

An experiment was also performed with a weighting of 0.875 where $\alpha_x(x, y, \sigma)$ and $\alpha_y(x, y, \sigma)$ were not in the desired range between 0 and 1 (instead of using the smaller estimate). The results were similar to those of the Method B_α, only more oscillatory, see Figure 7.5.
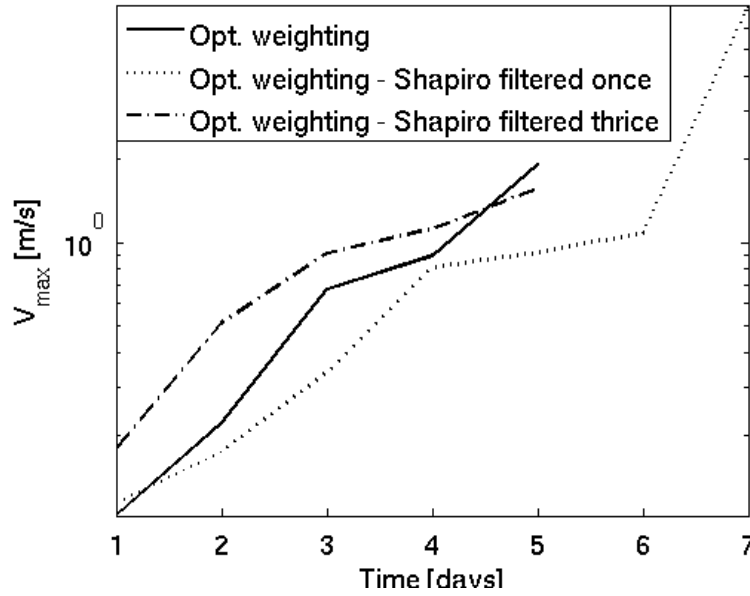
Figure 7.4: Maximum velocity for the optimal weighting approach, including no
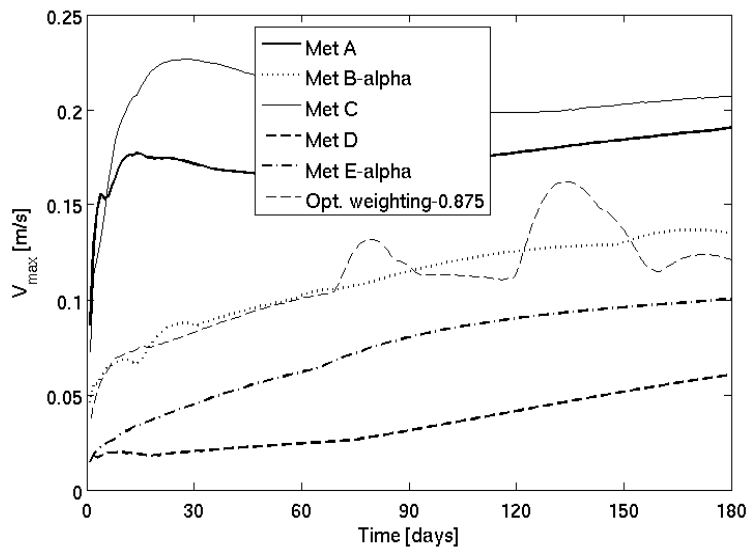Shapiro-filtering, and Shapiro-filtered once and thrice.

Figure 7.5: Maximum velocity for the methods, including optimal weighting -
version with fixed weight of 0.875 instead of smaller estimate.

7.3 The vorticity evolving in time

To observe the long-term behaviour of the errors, the depth-integrated vorticity

$$\int_{-1}^{0} \left[\frac{\partial v}{\partial x} - \frac{\partial u}{\partial y} \right] d\sigma \ ,$$

was plotted over a time span of 100 days for the standard 2nd order POM (Method A), see Figure 7.6.

A pattern of eight vortices, four cyclonic and four anticyclonic, is established around Day 20. This pattern seems to represent a stable state, where the SESK errors cease to grow. This agrees with the error observed in the kinetic energy and maximum velocity, see Figures 7.1 and 7.2.

To illustrate the clear connection between the initial acceleration of the vorticity, and the strength of the later vorticity, the corresponding results for Method D is included (Figure 7.7). Note that the vorticity errors are one order of magnitude smaller than for the Method A. Apart from this, the same stagnation of the error growth can be observed.

The depth-integrated vorticity for the unstable optimal weighting (without Shapiro filtering) is included in Figure 7.8, showing the five days before the run is terminated. The chaotic picture is a clear contrast to the 'smooth' vortices resulting from Method A and D.

7.4 Comparison to the methods from [Berntsen and Oey, 2010]

A good way of measuring the value of the methods obtained here, is to consider the finite difference methods that already have been used for the Princeton Ocean Model. Since the setup used in [Berntsen and Oey, 2010] is also utilised in this study, a comparison is permitted.

The study of the plots of the kinetic energy and maximum velocity (e.g. Figures 7.1 and 7.2), reveals that the best method of 4th order obtained here, Method D, has an error comparable to the well-known 4th order McCalpin method [McCalpin, 1994], [Berntsen and Oey, 2010]. This indicates that a real breakthrough has not yet been made.

(a) Day 1

(b) Day 20

(c) Day 40

(d) Day 60

(e) Day 80

(f) Day 100
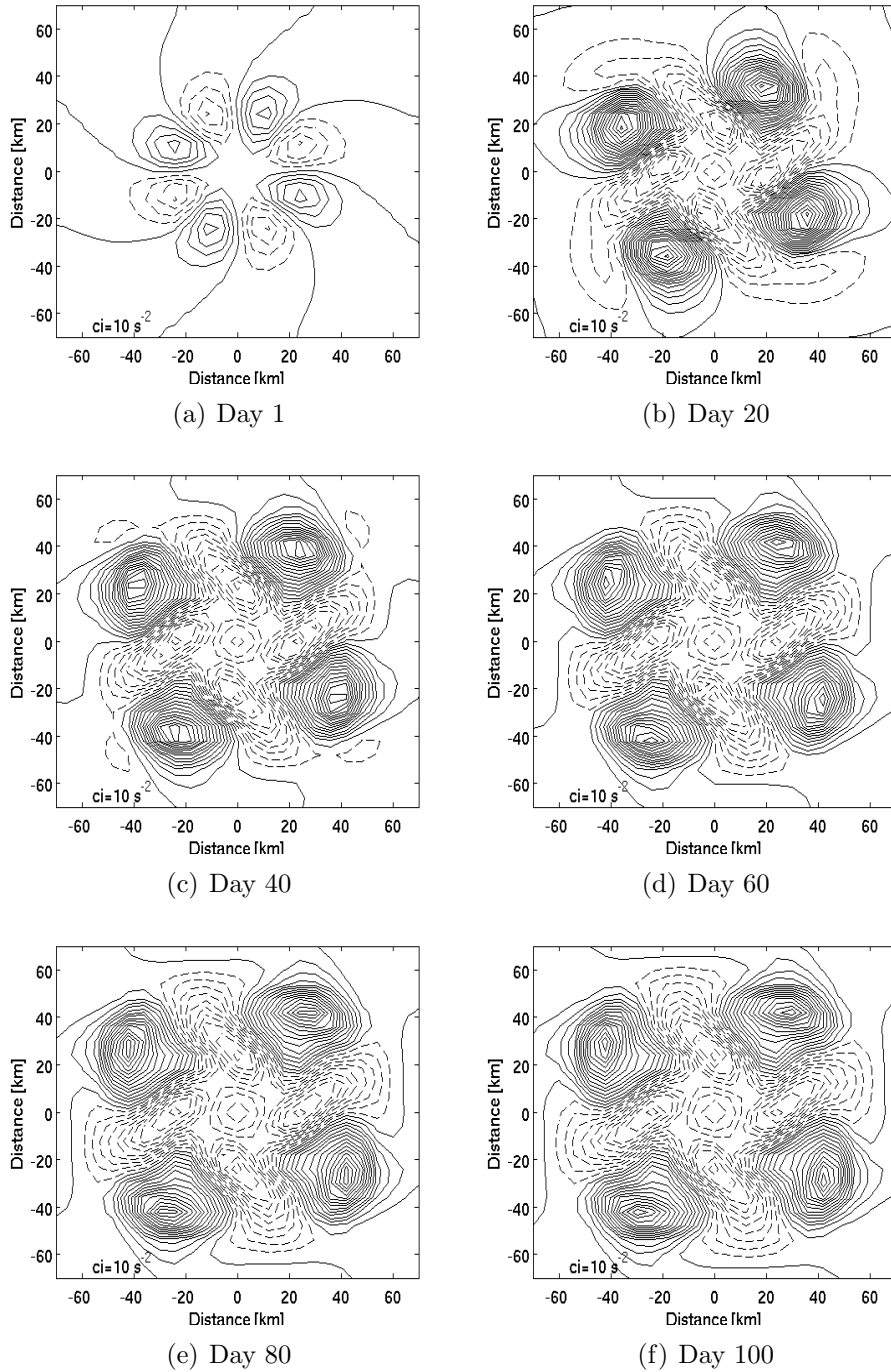
Figure 7.6: The depth-integrated vorticity for the standard 2nd order POM (Method A).

(a) Day 1

(b) Day 20

(c) Day 40

(d) Day 60

(e) Day 80

(f) Day 100
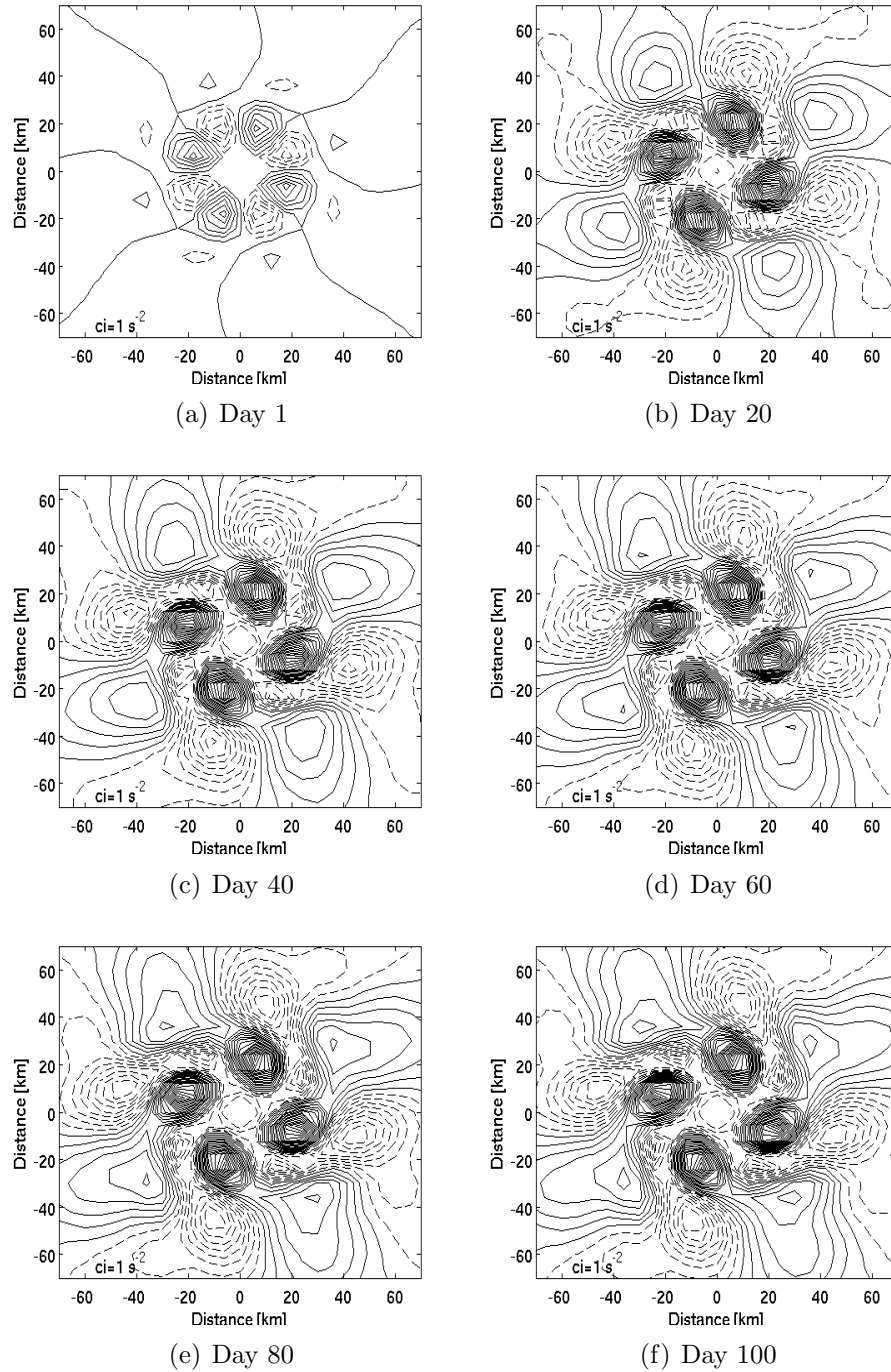
Figure 7.7: The depth-integrated vorticity for the Method D.

(a) Day 1

(b) Day 2

(c) Day 3
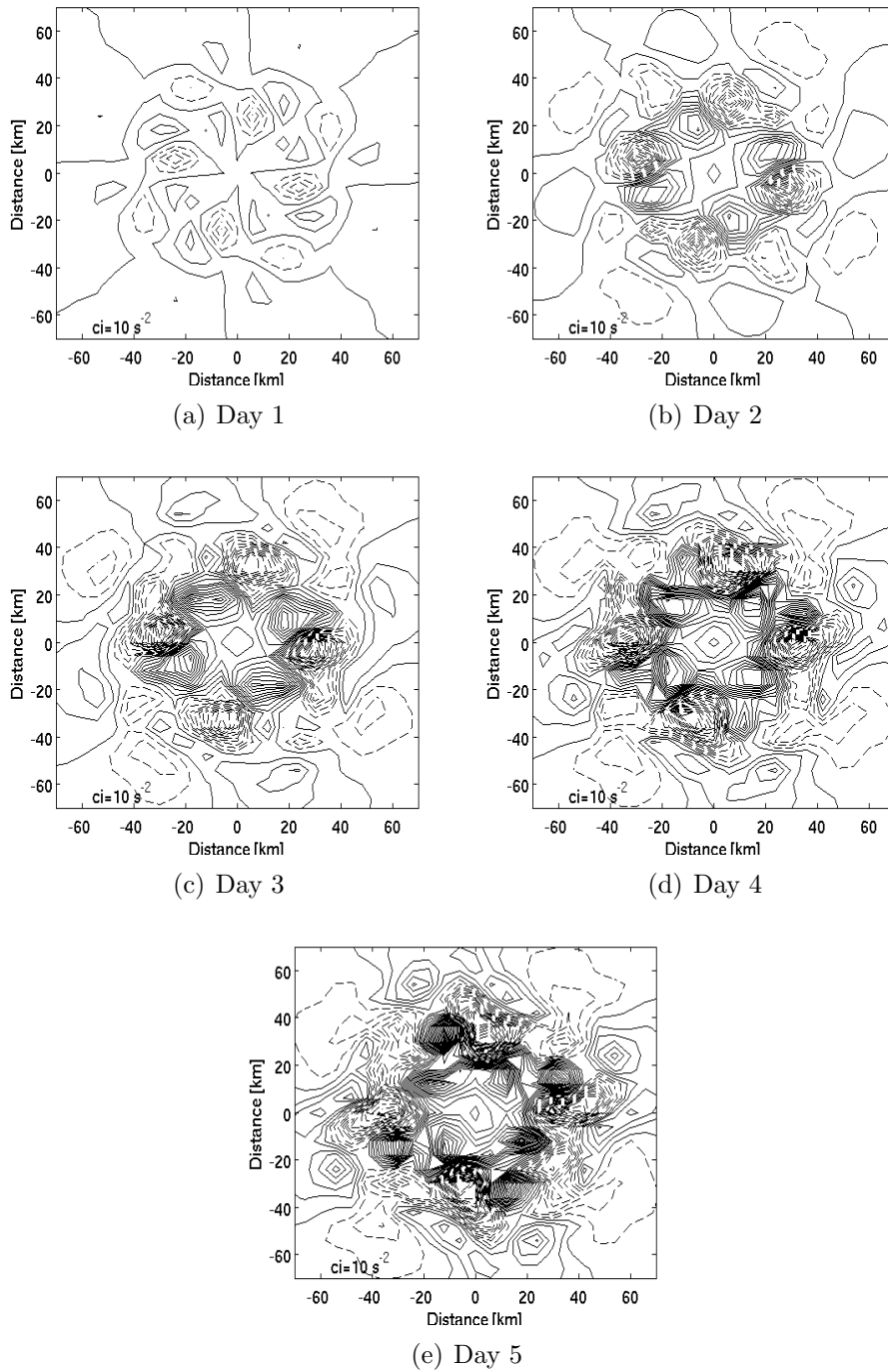
(d) Day 4

(e) Day 5

Figure 7.8: The depth-integrated vorticity for the optimal weighting (without Shapiro-filtering).

Chapter 8

Discussion

The error in the internal pressure gradient is one of the greatest concerns of the users of σ-coordinate ocean models. After the transformation to the terrain-following coordinates, the gradient consists of two terms, which are often both large and opposite of sign. Therefore, the estimation is vulnerable to the truncation errors of the numerical discretisation. Much effort has been put into finding new approaches, to reduce, and hopefully eliminate this problem entirely.

8.1   The finite volume approaches

To this end, a new family of finite volume methods has been developed, using the standard 2nd order POM as a starting point. During the process, the close relationship between the finite difference and finite volume approaches has been clearly demonstrated. The method of undetermined coefficients provided the fixed weights needed to take the methods to higher order. However, the expansion of the computational stencil did not always result in an approximation of the order that was sought initially.

The performances of the finite volume methods found in Chapter 2 turned out to be varying. Generally, they were either worse or only marginally better than the finite difference approaches of corresponding order. The work of Berntsen and Oey [2010] made a comparison possible. One should not underestimate the impact of the problem described in Section 2.4. If a way to overcome this could be found, perhaps the advantages of the finite volume approach would be more evident.

Furthermore, the method of undetermined coefficients is not the only way of producing new finite volume methods. A Taylor expansion approach could also be applied, and possibly give another set of methods with different, and

more advantageous properties.

8.2   The weighted approaches

The work of Thiem and Berntsen [2006] inspired an attack on the problem from a different angle: The internal pressure gradient was computed in a rotated grid, and the estimates were weighted with the standard 2nd order POM method, using a fixed constant. This approach made it possible to utilise the stencils from the finite volume study which previously did not lead to new methods.

The results for the weighted approaches were promising. The experiments with a fixed constant weight in Section 4.2 clearly displayed error reduction, which was consistent with the results from Thiem and Berntsen [2006]. This spurred the research in yet another direction; towards the optimal weighting approach.

The purpose of the optimal weighting was to create a field of weights that ideally would eliminate the internal pressure gradient error entirely. The weights should not vary in time, but in space, and be such that the pressure gradient would be set to zero when the methods gave estimates of comparable order and opposite signs. If not, the smaller value should be used.

Unfortunately, the first attempt at the optimal weighting was unsuccessful. The two methods did not seem to be able to interact in the desired way. Two estimates of opposite signs are needed to make the weighting effective, and this was only achieved in a few points. It does not necessarily follow that the optimal weighting is a fundamentally bad idea, only that the methods considered are ill-suited for the purpose. If a new pair of methods could be found, it would mean renewed hope for the approach.

But even if this could be achieved, it would be natural to expect that the optimal weighting will result in discontinuities in the internal pressure gradient. A possible solution could then be to use filtering techniques to smooth out the field. To investigate, some experiments were performed with Shapiro-filtering in all spatial dimensions. It was discovered that this can lead to 'false' weights between 0 and 1 – causing new disturbances.

One can argue that the optimal weights should vary in time, i.e. that an $\alpha_x(x, y, \sigma, t)$ should be computed at each time step. After all, the density profile is time-dependent. In this study, the weights were kept constant in time mainly for simplicity, and to reduce the computational cost. In addition, the initial errors are generally assumed to be closely correlated to the later errors. Even if the error cancellation should happen to be a little inaccurate,

the approach should, if successful, improve the results in any case.

8.3   Concluding remarks

Beyond doubt, the idea of weighting is enticing. The hope that in combining two schemes, the best of two worlds can be achieved at the same time, is both intuitive and accessible.

Instead of limiting the weighting to the horizontal, consider the possibility of using weighting in the vertical to reduce the internal pressure gradient error. Some work on this has been done before, for instance Song [1998] suggested the use of a vertically weighted Jacobian when computing gradients.

As mentioned before, Stelling and Van Kester [1994] constructed a new method of computing the internal pressure gradient by interpolating the derivatives back to z-coordinates. As a consequence, it was ensured that for a test case with a density field that only varies in z, the numerical solution would equal the analytical solution. The approach can be interpreted as a sort of optimal weighting in the vertical. Even though the method may have other short-comings [Slørdal, 1997], the idea in itself is interesting.

It is clear that the two terms resulting from the transformation to σ-coordinates in expression (1.9), should cancel out in the case of horizontal isopycnals. To exploit this, one can imagine that an alternative sort of optimal weighting can be found, by the means of any sort of adjustment of the approximations in the given terms. Vertical interpolation is just one possibility. Similarly to the attempted optimal weighting in the horizontal, the weights will then be determined by demanding that the pressure gradient is zero when this is given by the analytical solution. The challenge will be how to carry out the idea, while still satisfying the need for consistency and stability.

The discussion here is mainly based on the results of experiments. A closer look at the error terms of the different methods could probably offer additional analytical insight, and consequently more fundamental explanations to the performances of the different methods. It is clear that both approaches have the potential to reduce the internal pressure gradient. The actual execution of the ideas, however, requires further efforts.

In addition, some errors will not show in idealised test cases, and therefore more realistic tests should be applied in order to fully understand the value of new approaches. Certain methods will even perform better when used in a more realistic context. For example, the use of more points can potentially give more robust approximations in the presence of a rougher bottom topography, and this advantage is not revealed by the present seamount case.

One should keep in mind that new approaches can introduce new sources of errors. For instance, whenever interpolation is utilised, one must take the inaccuracies produced by this into consideration as well. It is important to always weigh the improvement in one area up against what could be lost in another.

Bibliography

Backhaus, J. and Hainbucker, D. (1987). A finite difference circulation model for shelf seas and its application to low freqency varibility on th North European Shelf. In Nihoul, J. and Jamart, B., editors, *Three-Dimensional Models of Marine and Estuarine Dynamics*, pages 221–244. Elsevier, Oceanography Series 45.

Barnier, B., Marchesiello, P., de Miranda, A., Molines, J.-M., and Coulibaly, M. (1998). A sigma-coordinate primitive equation model for studying the circulation in the South Atlantic. Part I: Model configuration with error estimates. *Deep-Sea Research I*, 45:543–572.

Beckmann, A. and Haidvogel, D. (1993). Numerical simulation of flow around a tall isolated seamount. Part I: Problem formulation and model accuracy. *Journal of Physical Oceanography*, 23:1736–1753.

Berntsen, J. (2000). USERS GUIDE for a modesplit σ-coordinate numerical ocean model. Technical Report 135, Dept. of Applied Mathematics, University of Bergen, Johs. Bruns gt.12, N-5008 Bergen, Norway. 48p.

Berntsen, J. (2002). Internal pressure errors in sigma-coordinate ocean models. *Journal of Atmospheric and Oceanic Technology*, 19(9):1403–1414.

Berntsen, J. and Oey, L. (2010). Estimation of the internal pressure gradient in -coordinate ocean models: comparison of second-, fourth-, and sixth-order schemes. *Ocean Dynamics*.

Bleck, R. and Smith, L. (1990). A wind-driven isopycnic coordinate model of the North and Equatorial Atlantic Ocean. I - Model development and supporting experiments. *Journal of Geophysical Research*, 95:3273–3285.

Blumberg, A. and Mellor, G. (1987). A description of a three-dimensional coastal ocean circulation model. In Heaps, N., editor, *Three-Dimensional Coastal Ocean Models*, volume 4 of *Coastal and Estuarine Series*, pages 1–16. American Geophysical Union.

Bryan, K. and Cox, M. (1968). A nonlinear model of an ocean driven by wind and differential heating: Parts I and II. *J. Atmos. Sci.*, 25:945–978.

Chen, C., Liu, H., and Beardsley, R. (2003). An Unstructured Grid, Finite-Volume, Three-Dimensional, Primitive Equations Ocean Model: Application to Coastal Ocean and Estuaries. *Journal of Atmospheric and Oceanic Technology*, 20:159–186.

Chu, P. and Fan, C. (1997). Sixth-order difference scheme for sigma coordinate ocean models. *Journal of Physical Oceanography*, 27:2064–2071.

Cushman-Roisin, B. (1994). *Introduction to Geophysical Fluid Dynamics*. Prentice Hall. ISBN-0-13-353301-8.

Gary, J. (1973). Estimation of truncation errors in transformed coordinate, primitive equation atmospheric models. *Journal of Atmospheric Science*, 30:223–233.

Gill, A. (1982). *Atmosphere-Ocean Dynamics*. Academic Press.

Haidvogel, D. and Beckmann, A. (1999). *Numerical ocean circulation modeling*, volume 2 of *Series on Environmental Science and Management*. Imperial College Press.

Haney, R. (1991). On the pressure gradient force over steep topography in sigma coordinate ocean models. *Journal of Physical Oceanography*, 21:610–619.

Kundu, P. and Cohen, I. (2004). *Fluid Mechanics*. Elsevier Academic Press.

LeVeque, R. (2002). *Finite-Volume Methods for Hyperbolic Problems*. Cambridge University Press.

Marsaleix, P., Auclair, F., and Estournel, C. (2009). Low-order pressure gradient schemes in sigma coordinate models: The seamount test revisited. *Ocean Modelling*, 30:169–177.

McCalpin, J. (1994). A comparison of second-order and fourth-order pressure gradient algorithms in a σ-coordinate ocean model. *International Journal for Numerical Methods in Fluids*, 18:361–383.

Mellor, G. (2003). Users guide for a three-dimensional, primitive equation, numerical ocean model. Technical report, Princeton University.

Mellor, G., Ezer, T., and Oey, L.-Y. (1994). The pressure gradient conundrum of sigma coordinate ocean models. *Journal of Atmospheric and Oceanic Technology*, 11:1126–1134.

Mellor, G., Oey, L.-Y., and Ezer, T. (1998). Sigma coordinate pressure gradient errors and the seamount problem. *Journal of Atmospheric and Oceanic Technology*, 15:1122–1131.

Ness, B. (2010). Sigma coordinate pressure gradient errors and the basin problem. Master's thesis, University of Bergen.

'ocean' (2010). *Encyclopedia Britannica.* Retrieved April 24, 2010, from Encyclopedia Britannica Online: http://www.britannica.com/EBchecked/topic/424285/ocean.

Pond, S. and Pickard, G. (1983). *Introductory Dynamic Oceanography*. Pergamon Press.

Roe, P. (1986). Characteristic-based schemes for the Euler equations. *Ann. Rev.Fluid Mech.*, 18:337–365.

Shapiro, R. (1975). Linear filtering. *Mathematics of Computation*, 29:1094–1097.

Shchepetkin, A. and McWilliams, J. (2003). A method for computing horizontal pressure-gradient force in an oceanic model with a non-aligned vertical coordinate. *Journal of Geophysical Research*, 108(C3, 3090):doi:10.1029/2001C001047.

Slørdal, L. (1997). The Pressure Gradient Force in Sigma-Co-ordinate Ocean Models. *International Journal for Numerical Methods in Fluids*, 24:987–1017.

Song, Y. (1998). A general pressure gradient formulation for ocean models. Part I: Scheme design and diagnostic analysis. *Monthly Weather Review*, 126:3213–3230.

Song, Y. and Haidvogel, D. (1994). A semi-implicit ocean circulation model using a generalized topography-following coordinate system. *J.Comp.Phys.*, 115:228–244.

Stelling, G. and Van Kester, J. (1994). On the approximation of horizontal gradients in sigma coordinates for bathymetry with steep bottom slopes. *International Journal for Numerical Methods in Fluids*, 18:915–935.

Thiem, Ø. and Berntsen, J. (2006). Internal pressure errors in sigma-coordinate ocean models due to anisotropy. *Ocean Modelling*, 12:140–156.

Yang, H. and Przekwas, A. (1992). A comparative study of advanced shock-capturing schemes applied to Burgers equation. *Journal of Computational Physics*, 102:139–159.